How does the air-sea coupling frequency affect convection during the MJO passage?

Ning Zhao[1] and Tomoe Nasuno[2]

[1]Japan Agency for Marine-Earth Science and Technology
[2]Frontier Reserach Center for Global Change

November 23, 2022

Abstract

The importance of air-sea coupling in the simulation and prediction of the Madden-Julian Oscillation (MJO) has been well established. However, it remains unclear how air-sea coupling modulates the convection and related oceanic features on the subdaily scale. Based on a regional cloud-resolving coupled model, we evaluated the impact of the air-sea coupling on the convection during the active phase of the MJO by varying the coupling frequency. The model successfully reproduced the atmospheric and oceanic variations observed by satellite and measurements but with some quantitative biases. According to the sensitivity experiments, we found that stronger convection was mainly caused by the higher sea surface temperatures (SSTs) generated in highly coupled experiments, especially when the coupling frequency was 1 hour or shorter. A lower coupling frequency would generate the phase lags in the diurnal cycle of SST and related turbulent heat fluxes. Our analyses further demonstrated that the phase-lagged diurnal cycle of SST suppressed deep convection through a decrease in daytime moistening in the lower troposphere. Meanwhile, in the upper ocean, the high-frequency air-sea coupling helped maintain the shallower mixed and isothermal layers by diurnal heating and cooling at the sea surface, which led to a higher mean SST. In contrast, the barely coupled experiments underestimated SST and therefore convective activities. Overall, our results demonstrated that high-frequency air-sea coupling (1 hour or shorter) could improve the reproducibility of the intensity and temporal variation in both diurnal convection and upper ocean processes.

How does the air-sea coupling frequency affect convection during the MJO passage?

Ning Zhao[1], **Tomoe Nasuno**[1]

[1]Japan Agency for Marine Earth Science and Technology, Yokosuka, Kanagawa, Japan

Key Points:

- High-frequency air-sea coupling improves the reproducibility of both convection and upper ocean processes
- Low-frequency coupling causes phase-lagging in diurnal cycle
- Higher daytime SST is more important than the daily mean

Corresponding author: N. Zhao, `zhaoning@jamstec.go.jp`

Abstract

The importance of air-sea coupling in the simulation and prediction of the Madden-Julian Oscillation (MJO) has been well established. However, it remains unclear how air-sea coupling modulates the convection and related oceanic features on the subdaily scale. Based on a regional cloud-resolving coupled model, we evaluated the impact of the air-sea coupling on the convection during the active phase of the MJO by varying the coupling frequency. The model successfully reproduced the atmospheric and oceanic variations observed by satellite and *in situ* measurements but with some quantitative biases. According to the sensitivity experiments, we found that stronger convection was mainly caused by the higher sea surface temperatures (SSTs) generated in highly coupled experiments, especially when the coupling frequency was 1 hour or shorter. A lower coupling frequency would generate the phase lags in the diurnal cycle of SST and related turbulent heat fluxes. Our analyses further demonstrated that the phase-lagged diurnal cycle of SST suppressed deep convection through a decrease in daytime moistening in the lower troposphere. Meanwhile, in the upper ocean, the high-frequency air-sea coupling helped maintain the shallower mixed and isothermal layers by diurnal heating and cooling at the sea surface, which led to a higher mean SST. In contrast, the barely coupled experiments underestimated SST and therefore convective activities. Overall, our results demonstrated that high-frequency air-sea coupling (1 hour or shorter) could improve the reproducibility of the intensity and temporal variation in both diurnal convection and upper ocean processes.

Plain Language Summary

The Madden-Julian Oscillation (MJO) is one of the important sources of atmospheric variability in tropical regions, however, even the modern numerical models could not well reproduce the MJO. We believe that the underestimation of air-sea coupling may cause some parts of such biases in simulating/predicting the MJO. Therefore, our study is aimed to uncover the impact of the air-sea coupling on convection and the related oceanic feature during the MJO. By varying the air-sea coupling frequency, our results showed that the 1-hour or higher frequency coupled experiments had better performance due to the well-reproduced sea surface temperature (SST), while suppressed convection was found in barely coupled experiments. In general, our study suggested that the high-frequency air-sea coupling could improve the reproducibility of both convection and upper ocean features during the MJO.

1 Introduction

The Madden-Julian Oscillation (MJO) is the chief source of variability in tropical regions on the intraseasonal time scale, which features an eastward propagating convectively active envelope (Madden & Julian, 1972). Over the decades, increasing evidence has shown that the MJO not only influences the global climate system but also many types of extreme weather in the tropics and midlatitudes (e.g., Kayano & Kousky, 1999; Kessler, 2001; Lorenz & Hartmann, 2006; Zhang, 2013; Wang & Moon, 2018). Therefore, it is crucial to obtain the successful simulation/prediction of the MJO for tropical weather systems, extreme weather events, monsoons, and the El Nio-Southern Oscillation (Vitart, 2014; Mishra et al., 2017; Wu et al., 2019).

To successfully simulate/forecast the MJO, numerous studies have been carried out; however, some systematic biases remained even in the state-of-the-art climate and forecast models due to the complexities of the MJO (e.g., Madden & Julian, 2005; Peatman et al., 2014; DeMott et al., 2015; Pilon et al., 2016; Kim et al., 2018). Recent studies found that the moistening processes are crucial to the initiation of the MJO and its maintenance/propagation (e.g., Raymond & Fuchs, 2009; Ruppert & Johnson, 2015; Tseng et al., 2015; Nasuno et al., 2015). For example, based on a regional numerical model, Hagos et al. (2011) demonstrated the important role of the moistening process on stratiform heating and related potential temperature perturbations, and their results also indicated the essence of well-represented shallow- and deep-convection in simulating the MJO. Other studies have mentioned the potential effect of preconditioning moistening on MJO-related rainfall, although the effect may depend on events (e.g., Zermeo-Daz et al., 2015; Chen & Zhang, 2019).

It is now well known that the MJO is a highly air-sea coupled phenomenon from the intraseasonal scale to the subdaily scale (e.g., Waliser et al., 1999; Zhang & Anderson, 2003; DeMott et al., 2015, and the references therein). Numerous studies have demonstrated that the inclusion of air-sea coupling improves the reproducibility of moistening processes during MJO (e.g., Fu et al., 2013; Seo et al., 2014). For example, Kim et al. (2010) suggested that air-sea coupling could improve the intensity and spatiotemporal evolution of the MJO. Seo et al. (2014) further confirmed the improved representation of diurnal sea surface temperature (SST) and the buildup of preconvection warming and moistening in highly coupled models. Based on the *in situ* observations, Ruppert and Johnson (2015) demonstrated that diurnally varying SST could invigorate net column moistening aloft. Some recent studies also suggested that the feedback of SST (hence, air-sea coupling) maintained propagation of the MJO (e.g., Webber et al., 2010; Zhu et al., 2017).

Although the importance of air-sea coupling on convection and the MJO has been well established, few studies have examined detailed modulations on the diurnal scale (e.g., Neale & Slingo, 2003; Crueger et al., 2013; Green et al., 2017). Whats more, some studies have also shown that the air-sea coupling frequency may modulate the reproducibility of the diurnal cycle of SST (e.g., Shinoda, 2005; Seo et al., 2014). It is reasonable to expect that the modulated SST may further influence the subdaily moistening processes and the MJO (e.g., Ruppert & Johnson, 2015; Hagos et al., 2016; Katsumata et al., 2018). However, such modulations on the SST by air-sea coupling were neglected in most studies and, therefore, remained unclear.

Thus, the goal of this study is to evaluate the effect of air-sea coupling (and the coupling frequency) on convective activities and related upper oceanic variations, especially on the subdaily scale. As part of the ongoing Year of the Maritime Continent (YMC) project (Yokoi et al., 2017, 2019; Nasuno, 2019; Wu et al., 2019), we focus on one MJO event (November 26th to December 4th, 2017; Figure 1b) captured during the YMC-Sumatra 2017 field campaign. In this period, a large number of land- and ship-based *in situ* observations are available, providing a great opportunity to validate the capability of our numerical experiments.

This paper is organized as follows. Section 2 includes descriptions of the model setup, data source and sensitivity experimental designs. Section 3 includes validation of the model performance with and without cumulus parameterizations. Section 4 documents the impact of coupling frequencies on the convection and surface conditions, along with analyses of the heat and moisture budgets. In Section 5, the role of the daily mean SST and how the SST was modulated by the coupling frequency are discussed. Finally, a summary of the major findings is presented in Section 6. Results on the cumulus parameterizations and extra experiment for the role of local SST are presented in Sections S1 and S2 in the Supporting Information Section.

2 Model and experiment settings

2.1 Model

In this study, numerical experiments were based on the Coupled-Ocean-Atmosphere-Wave-Sediment Transport (COAWST) Modeling System (Warner et al., 2010), and, for simplicity, we excluded the wave and sediment components and only activated the at-

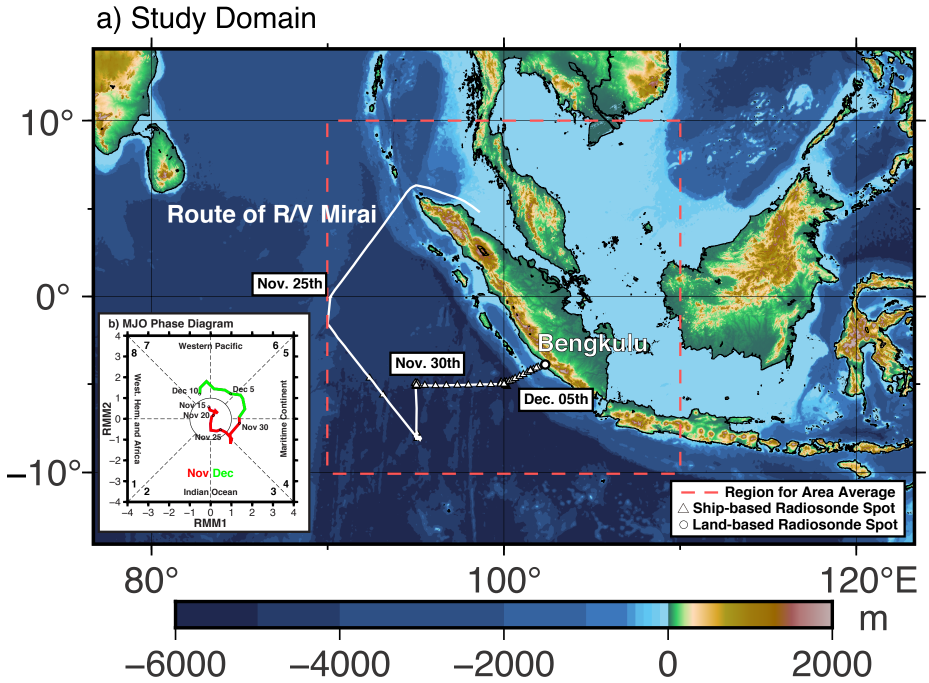

Figure 1. (a) Map of the study domain together with the route of R/V *Mirai* and the locations where the radiosonde was launched. The box enclosed by the red dashed line presents the Sumatra region for area averaging. The inner panel (b) presents the MJO RMM index obtained from the Bureau of Meteorology, Australia.

mospheric (Weather Research and Forecasting Model, WRF V4.1.2) and oceanic (Regional Ocean Modeling System, ROMS svn 980) components. In coupled experiments, WRF uses the SST calculated by ROMS, while ROMS receives heat fluxes, wind stress, surface temperature, relative humidity, and freshwater fluxes. In uncoupled experiments, WRF was activated alone using the satellite-based SST.

The model was designed to cover the region from 78°E to 122°E and 14°S to 14°N, where the center is located at Sumatra Island (0°, 100°E; Figure 1a). All simulations started at 0:00 UTC on November 21st and ran until 0:00 UTC on December 6th, which was 5 days prior to the active phase of the MJO over the Maritime Continent (Phase 4 & 5, Figure 1b).

The horizontal resolution of WRF and ROMS is 7 km with matching grids and land-sea masks (Nasuno 2019). The 30 s Global Multiresolution Terrain Elevation Data 2010 (Danielson & Gesch, 2011) and ETOPO1 (Amante & Eakins, 2009) were used for WRF and ROMS, respectively. WRF has 45 sigma layers from the surface to the top (50-hPa), and ROMS has 50 layers based on the quadratic Legendre polynomial function (Souza et al. 2015) with a larger number of vertical levels in the upper 50 m.

WRF uses the single-moment 7-class microphysics scheme (Bae et al., 2018), the Yonsei University PBL scheme (Hong et al., 2006), the Revised MM5 surface layer scheme (Jimnez et al., 2012), the Unified Noah Land Surface Model (Tewari et al., 2004), the RRTMG Shortwave and Longwave Schemes (Iacono et al., 2008), and the Grell-Freitas Ensemble (GFE) cumulus scheme (Grell & Freitas, 2014). ROMS uses the Mellor-Yamada Level-2.5 closure scheme associated with the third-order upstream horizontal advection, harmonic horizontal mixing, and 4th-order centered vertical advection, and no nudging term is included.

It is worth noting that at a so-called gray zone resolution (Gerard, 2007), the cumulus parameterization does not always enhance the reproducibility in our 7-km model. Therefore, we conducted extra experiments to obtain the best performance, and results can be found in the Supporting Information Section. The schemes we tested included the GFE scheme (Grell & Freitas, 2014), the New Simplified Arakawa-Schubert (NSAS) scheme (Kwon & Hong, 2017), and the Multiscale KainFritsch (MKF) scheme (Zheng et al., 2016). We also tested the New Tiedtke (NT) scheme (Zhang & Wang, 2017), which is not scale-aware but includes both deep and shallow cumulus components. Note that because the NSAS scheme does not have the shallow convection component, which was proved to be important in simulating convection (Pilon et al., 2016), we applied the Global/Regional Integrated Model system (GRIMs) shallow convection scheme (Hong & Jang, 2018) in CP1HC3 following Kwon and Hong (2017).

2.2 Data

In this study, the National Centers for Environmental Prediction (NCEP) Final (FNL) Operational Global Analysis data (NCEP, 2000) and Global Ocean Forecasting System (GOFS) 3.1 (Cummings, 2005) were used as the initial and lateral boundary conditions for WRF and ROMS, respectively. Additionally, in uncoupled experiments, the daily Optimum Interpolation SST (OISST) dataset was used for the lower boundary condition (Banzon et al., 2016; Reynolds et al., 2007). The modeled atmospheric and oceanic properties were saved every 1 hour over the course of each computation in all experiments.

For the model validation, we used precipitation data from the satellite-based hourly Global Rainfall Map (GSMaP) dataset together with ship-based [Research Vessel (R/V) *Mirai*] and land-based (Bengkulu, Indonesia) radiosonde data obtained during the YMC-Sumatra 2017 field campaign (Nasuno, 2019; Wu et al., 2019; Yokoi et al., 2019).

2.3 Sensitivity experiments of coupling frequency

To investigate the influence of the coupling frequency on convection during the MJO active phase, a set of experiments was carried out by varying the coupling interval from 30 minutes to 1 day and an uncoupled experiment (WRF-only). ROMS and WRF were coupled at the first-time step of each experiment and then coupled after the specified interval. For example, the 6-hourly coupled model would exchange atmospheric and oceanic information at 0:00 UTC, 6:00 UTC, 12:00 UTC, and 18:00 UTC. In addition, Three uncoupled (WRF-only) experiments were further conducted to discuss the role of daily mean SST (see subsection 5a and Section S2). Detailed descriptions of the sensitivity experiments can be found in Table 1.

3 Model validation

Figure 2 shows the horizontal distributions of the mean precipitation rates and maximum precipitation time during the active phase of the MJO (Nov. 26th-Dec. 4th) obtained by satellite and CP1HC. The heaviest rain occurred over the Gulf of Thailand near the eastern coast of the Malay Peninsula and the southern Andaman Sea (Burma Sea), along with a weak but widely distributed rainy zone covering the Indian Ocean and the Maritime Continent (Figure 2a). In the Southern Hemisphere, clear rainy zones were observed over the Indian Ocean, south of the equator and south of Java Island, but the precipitation rates were smaller. All the patterns mentioned above were successfully reproduced in CP1HC, although the rainy regions were not as concentrated as the observations in the Southern Hemisphere.

Table 1. Descriptions of sensitivity experiments

Experiment	Settings
CP30MC	30-min WRF-ROMS
CP1HC	1-h WRF-ROMS
CP3HC	3-h WRF-ROMS
CP6HC	6-h WRF-ROMS
CP12HC	12-h WRF-ROMS
CP1DC	1-d WRF-ROMS
NOCPC	WRF-only (OISST)
NOCPC+	WRF-only (OISST & daily mean SST from CP1HC)
NOCPC++	WRF-only (daily mean SST from CP1HC)

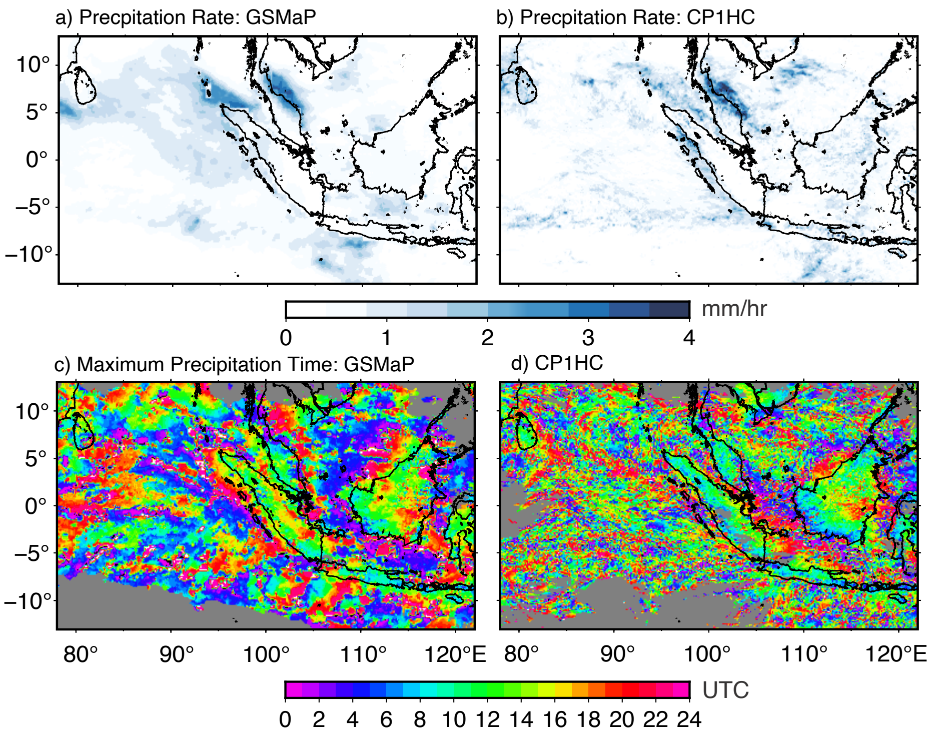

Figure 2. Horizontal distributions of precipitation rates and the time of maximum precipitation obtained from satellite observations (a and c) and CP1HC (b and d).

In addition to the precipitation rate, the time of maximum precipitation can also be regarded as an important indicator representing the diurnal cycle of precipitation. As shown in Figure 2c, the maximum precipitation mainly occurred in the evening near the coastal region and in the early morning inland (see the patterns over Sumatra and Kalimantan). Meanwhile, over the shallow coastal seas, the heaviest rain occurred in the early morning, especially near the Gulf of Thailand and west of Sumatra Island where the heaviest rainfall was observed. In general, the observed diurnal cycle he observed diurnal cycle was consistent with the diurnal cycle revealed in previous studies (Neale & Slingo, 2003; Mori et al., 2004). Moreover, in comparison with the observations, the precipitation in CP1HC reached its maximum rate at the same time (Figure 2d), although the simulated precipitation showed more small-scale features.

In addition, we further compared our model results with the *in situ* radiosonde profiles obtained during the YMC-Sumatra 2017 field campaign (Figure 3; also see Figure 1a for the locations of radiosonde observations). The atmosphere near Sumatra Island was dominated by the westerly wind over the entire active phase of the MJO, which could also be seen in the model. The meridional wind component (v) suggested that a transition of wind field occurred after Nov. 30th, as shown by the opposite meridional wind direction before and after the day. A similar transition of the meridional wind could also be found in our model, but with some underestimations. Moreover, both observations and simulations showed that very high relative humidity (RH) was dominant from the surface to the upper troposphere, indicating the vigorous convective activities occurred in both the model and real atmosphere.

Overall, our model showed good agreement with both satellite-based and *in situ* observations, suggesting that our model is reliable; therefore, we conducted sensitivity experiments of coupling frequencies using the same schemes and settings as CP1HC.

4 Results

4.1 The impact on the atmospheres

To examine the impact of the air-sea coupling frequency on convection, we first focused on the moisture and moisture fluxes in our sensitivity experiments. Figure 4a presents the map of the daily mean precipitable water (PW) and vertically integrated moisture fluxes averaged during the active phase of the MJO (from surface to 300-hPa, November 26th to December 4th) in CP1HC. A large amount of PW was concentrated north of Sumatra Island and the Malay Peninsula, which consists of the location of the heaviest rainfall, as observed by satellite and CP1HC (Figure 2). The cyclonic gyre located in both north and south of the equator, associated with the jet-like moisture fluxes originating from the Indian Ocean to the west (also from the South China Sea), exhibited the existence of vigorous convective activities over the Maritime Continent (i.e., the active phase of the MJO).

In comparison with CP1HC, the differences in the mean PW and moisture fluxes were not obviously changed in CP30MC, CP3HC, or CP6HC. However, unlike the highly coupled experiments (i.e., 6 hours or more coupled), the total amount of PW decreased by 5 mm or more in most regions in the barely coupled models, with the clearest pattern in the uncoupled experiment (NOCPC, Figure 4g). Meanwhile, the moisture flux anomalies showed anticyclonic gyre-like and westward jet-like patterns, indicating greatly suppressed convective activities (Figure 4e-g). Note that although the anticyclonic gyre-like pattern could also be seen in Figure 4d, no westward anomalies were found, suggesting that the convection was weakened in the CP6HC but not as much as that in the barely coupled/uncoupled experiments.

Figure 5a presents the frequency-altitude distributions of RH over the seas near Sumatra Island (red box in Figure 1a; Nasuno et al. 2015). The lower troposphere (sur-

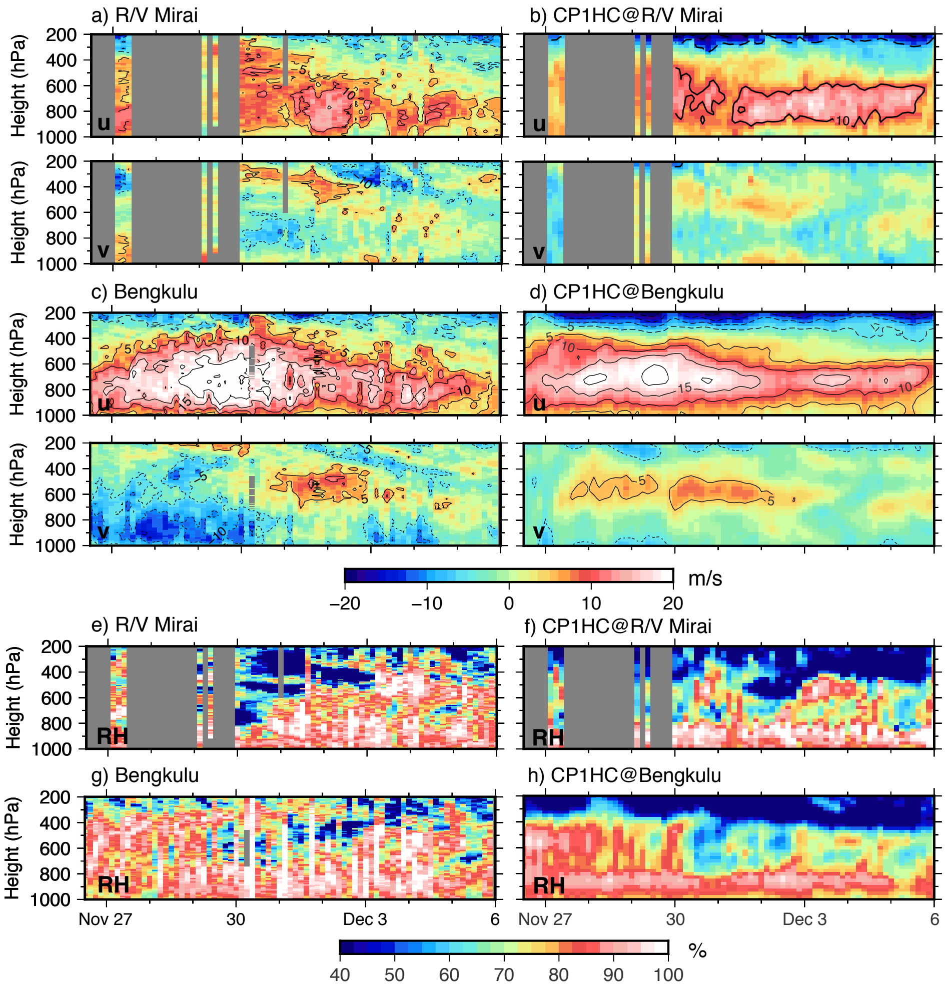

Figure 3. Vertical profiles of wind and relative humidity obtained by CP1HC and radiosonde observations obtained during the YMC-Sumatra 2017 field campaign.

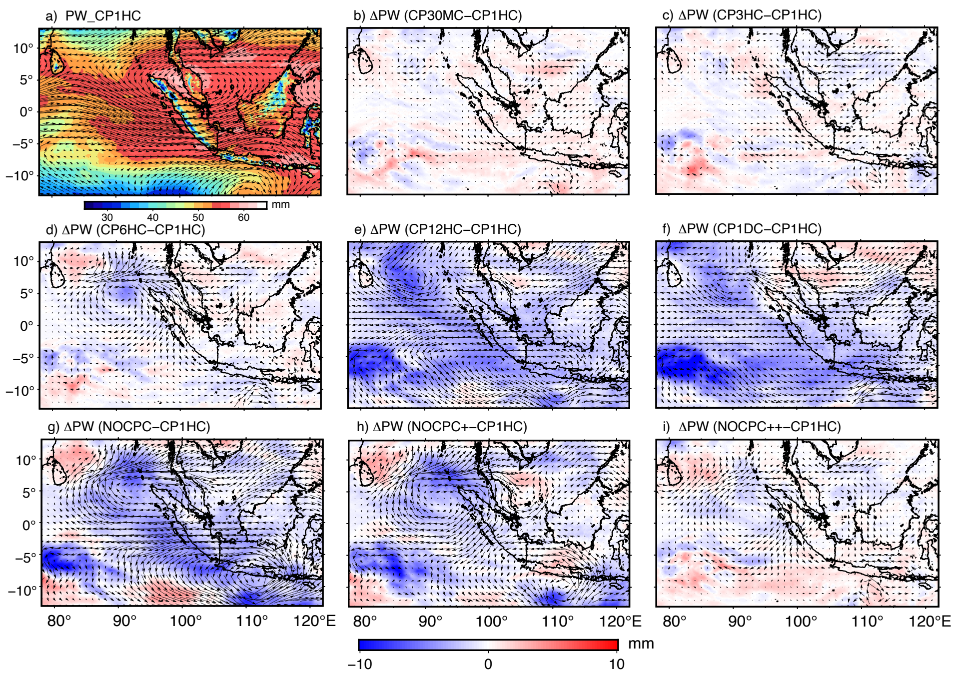

Figure 4. Horizontal distributions of the precipitable water and moisture fluxes integrated from the surface to 300-hPa height during the active phase of the MJO (November 26th to December 4th) in (a) CP1HC and (b-h) the differences between CP1HC and other runs.

face to 800-hPa level) was characterized by frequent occurrences of 80-100% RH. The frequency in the middle troposphere (850-500 hPa) ranged from 50% to 100% RH, where 70-80% RH occurred the most. Above the 500-hPa level, the atmosphere became increasingly dier as the height increased. The other highly coupled experiments showed only small differences (Figure 5b-d) from CH1HC. In the 30-minute coupled experiment, the increased (decreased) frequency of $> 70\%$ RH ($< 70\%$ RH) suggested that the convective activities were more enhanced. However, this was not the case in the barely coupled/uncoupled experiments. The occurrences of $> 70\%$RH (hereafter, high RH) were greatly reduced from the lower troposphere to the upper levels, and $>90\%$ RH was nearly extinct in the midlevels (Figure 5e-g). Accordingly, low RH appeared more frequently in nearly the entire column above the atmospheric boundary layer in the barely coupled/uncoupled experiments, suggesting that convection was greatly weakened.

One may consider that the reduction in high RH may be caused by the modulated preconditioning of the MJO (e.g., Seo et al. 2014). However, our models showed different results. As shown in Figure 6, the occurrences of high RH ($>70\%$) showed no significant differences before the MJO, even at in midlevels (Figure 6c). Nevertheless, the situation started to change only after the MJO entered phase 4 (November 26th-30th, Figure 1b), although the SSTs had already been modulated since the model initiation (see Figure S3 in the Supporting Information). In particular, the atmosphere was greatly moistened in the highly coupled experiments ($> 90\%$ occurrence of high RH), which consisted of the vigorous convection during the MJO. Nonetheless, the barely coupled/uncoupled experiments showed relatively lower values, as suggested by the clear separation in the middle troposphere among the experiments. The occurrence of high RH in the barely coupled/uncoupled experiments was approximately 10% lower than that in the highly coupled experiments. As the MJO propagated to the east (after December 1st, i.e., phase 5 of the MJO), convection was suppressed in all experiments (see the descending trend

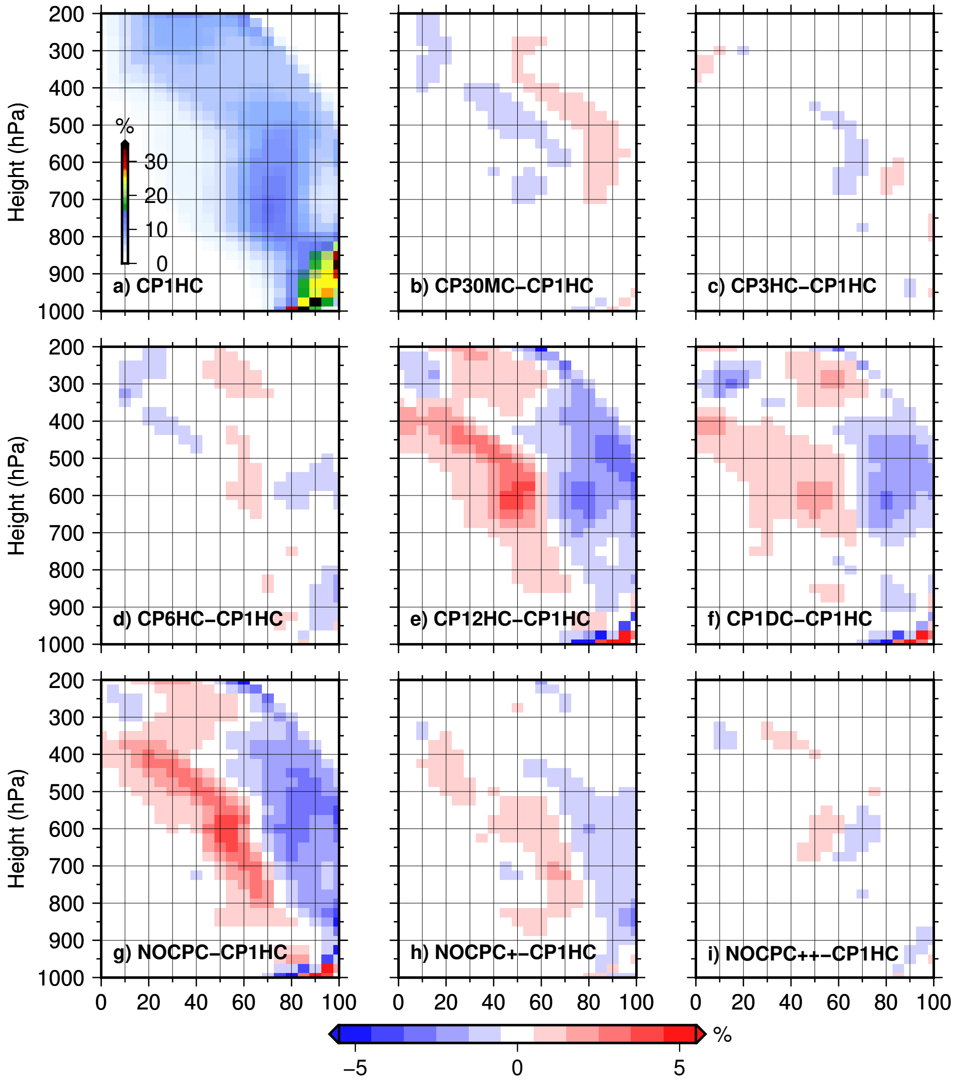

Figure 5. The frequency-altitude distributions of the simulated relative humidity over the seas around Sumatra Island (10°S-10°N, 90°-110°E; red box in Figure 1a).

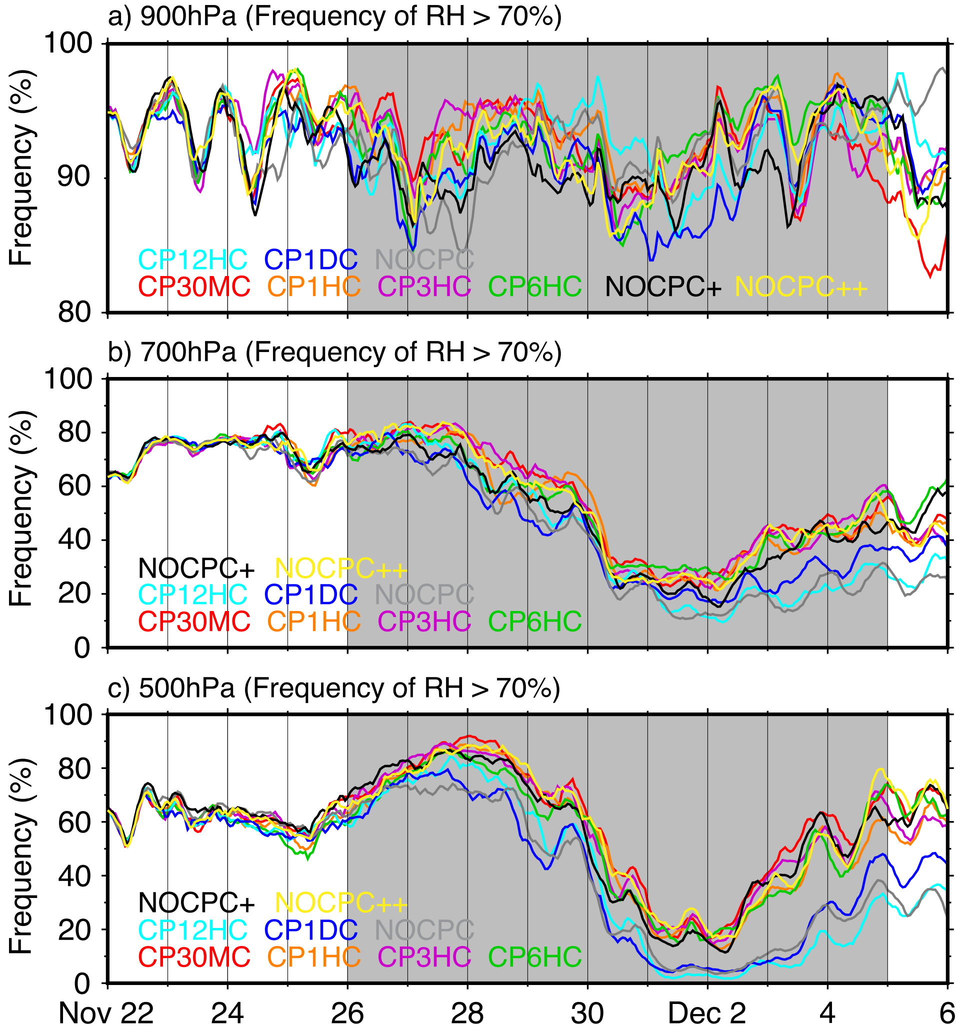

Figure 6. Time series of frequencies (occurrences) of the grid with high relative humidity (> 70%) at the (a) 900-hPa level, (b) 700-hPa level, (c) 500-hPa level, and time series of (d) vertical accumulated divergence of moisture fluxes from the surface to the 800-hPa level.

in Figure 6), but the differences became larger. Overall, our results suggested that the high-frequency air-sea coupling enhanced the convective activities during the active phase of the MJO, and it also helped with the maintenance of the moist atmosphere after the MJO passed.

4.2 Modulated diurnal cycle at the sea surface

Figure 7 represents the diurnal composite of surface variables averaged in the Sumatra region (red box in Figure 1a and ocean only). The SSTs reached over 29.5 °C in the highly coupled experiments, along with a clear diurnal cycle that was absent in the barely coupled/uncoupled experiments. Although the daily mean SST and its diurnal amplitude were nearly identical among the highly coupled experiments (Table 2), the temporal variations were not. In CP1HC and CP30MC, the largest SST appeared at 8:00 UTC, which consisted of a recent study based on buoy data (Morak-Bozzo et al., 2016). However, this was not the case in CP3HC (CP6HC), where the diurnal cycle of SST was de-

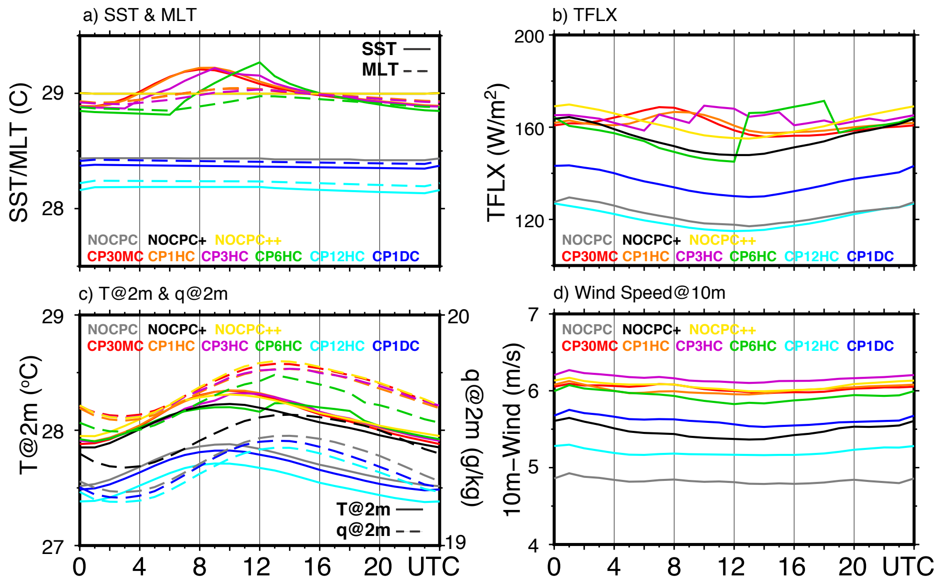

Figure 7. Diurnal composites of (a) sea surface temperature (solid line) and mixed-layer temperature (dashed line), (b) turbulent heat fluxes (the sum of surface sensible and latent heat fluxes, upward positive), (c) surface air temperature (solid line) and specific humidity (dashed line) at 2 m, and (d) surface wind speed at 10 m. Colors represent different experiments. Note that the correspondence of color and experiment is consistent in this paper, except Figure 14.

layed by 1 hour (4 hours). On the other hand, CP12HC and CP1DC did not have any diurnal cycle of SST, and the mean values were also lower than those of highly coupled experiments.

The surface turbulent heat fluxes (TFLX; upward positive), which are mainly controlled by the latent heat flux (see Figure S5 in the Supporting Information), had more complex variations. The TFLX in CP30MC started increasing at 16:00 UTC and finally reached its maximum at 7:00 UTC (14:00 LT in the Sumatra region), followed by a 9-hour decrease. Similar variations could be found in CP1HC, although its largest TFLX appeared 1 hour later and smaller. The lag became larger in CP3HC, along with a 2-hour period fluctuation caused by the different response times of surface air temperature (T2m) and specific humidity (q2m) (Figure 7c; also see Figure 13d for the lead-lag correlation).

Among the highly coupled experiments, CP6HC showed totally different trends: the TFLX monotonically decreased during the daytime and then suddenly increased after 12:00 UTC. Such unrealistic variations were generated by the coupling procedure used in our model. Except for the time step of coupling, both WRF and ROMS used a constant boundary forcing at most of the time steps. For example, in the CP6HC, the increasing SST from 6:00 UTC to 12:00 UTC only occurred in the ocean (ROMS), while WRF used the temporally constant SST (which was obtained at 6:00 UTC) until the next coupling time. Therefore, the underestimation and overestimation occurred continuously due to the constant forcing.

Unlike the SST and TFLX, the surface air temperature (T2m) and specific humidity experienced the same diurnal cycle in all experiments, although they were 0.5 °C and 0.25 g/kg higher in the highly coupled experiments (Figure 7c). Despite the unique vari-

Table 2. Daily Mean SST and TFLX in the Sumatra Region

Experiment	SST (°C)	TFLX (W/m^2)
CP30MC	29.02	161.04
CP1HC	29.02	161.30
CP3HC	29.01	163.85
CP6HC	28.96	158.55
CP12HC	28.17	120.02
CP1DC	28.36	135.95
NOCPC	28.43	122.22
NOCPC+	29.00	155.03
NOCPC++	29.00	161.87

ations in CP6HC, the heating of surface air started at 1:00 UTC, leading to the highest T2m at 9:00 UTC. The increase in q2m started slightly later at 3:00 UTC and then reached its maximum at 13:00 UTC (Figure 7c).

The surface wind speed had nearly no diurnal cycle regardless of coupling frequencies, but it was 1 m/s higher in the highly coupled experiments (Figure 7d). Note that the bimodal variations in T2m and its earlier increase than the SST in the CP6HC were mainly caused by phase-delayed heating from the ocean after 12:00 UTC, which alleviated the nighttime temperature decrease.

Without the diurnally varying surface forcing, the SSTs were nearly constant in the barely coupled experiments. Unlike the increasing trends during the daytime in the highly coupled experiments, their TFLXs decreased during the daytime and increased during the nighttime, following T2m and q2m with an opposite sign (Figure 7c). Such variations were similar to the uncoupled experiment (NOCPC). Note that the higher SST and TFLX in CP1DC were caused by the nonzero solar radiation throughout the day, while the heating was updated to zero in CP12HC after 12:00 UTC (Figure 13c). Moreover, the influence of the mean SSTs and its diurnal cycle can be found in Section 5.

4.3 Heat and moisture budget analysis

To further elucidate the influence of the coupling frequency on subdaily moistening processes, we executed an area-averaged heat and moisture budget analysis. We rearranged the budget equations including the apparent heat source (Q1) and moisture sink (Q2) following Yanai et al. (1973):

$$\frac{\partial s}{\partial t} \equiv Q_1 - \vec{U} \cdot \nabla s - \omega \frac{\partial s}{\partial p}, \quad (1)$$

$$L_v \frac{\partial q}{\partial t} \equiv -Q_2 - L_v \vec{U} \cdot \nabla q - L_v \omega \frac{\partial q}{\partial p}, \quad (2)$$

where $s \equiv c_p T + gz$ is the dry static energy, c_p is the specific heat at constant pressure, T is the temperature, q is the specific humidity, L_v is the latent heat of condensation, and $\vec{U}$ and ω are the horizontal wind vector and the vertical wind component in pressure coordinates, respectively. All terms were calculated based on the hourly output from the model and averaged over the Sumatra region (ocean only, red box in Figure 1a) during the MJO active phase.

Figure 8 represents the diurnal composite time-altitude distributions of the s and q budgets averaged in the Sumatra region during the MJO active phase based on CP1HC. The atmosphere became warmer during the local daytime and cooler during the local nighttime, shifting its phase at 12:00 UTC (Figure 8a). On the other hand, diurnal moistening mainly occurred from 4:00 UTC (11:00 LT) at surface levels, and such moistening generally takes 4-5 hours to extend to the entire lower levels (Figure 8b). Although the positive Q1 could be seen all day long during the MJO, the strong heating started at 16:00 UTC (23:00 LT) in the middle troposphere and reached its maximum at 4:00 UTC (Figure 8c), while the corresponding moisture sink occurred slightly earlier at lower levels before the heating started (Figure 8d). Both Q1 and Q2 were basically balanced by vertical advection (s_{vadv} and q_{vadv}, Figure 8g and 9h, respectively), indicating the existence of vigorous convection, while horizontal moisture advection (q_{hadv}; Figure 8f) tended to dry the atmosphere due to the background eastward moisture fluxes during the MJO (Figure 4a). Note that, in this study, we only focused on the air-sea interaction and convection above the ocean, so that the time evolutions of Q1 and Q2 may include some influences from the diurnal land-sea circulation; however, such influences were neglected during the analyses.

Although the differences between CP6HC and CP1HC were small in the PW and high RH occurrences (Figures 4 and 5), the budget analyses showed more detailed modulations. It is easy to find that the heating (moistening) was stronger (weaker) during the nighttime (daytime) in the CP6HC (Figures 9a and 9b), which was likely due to the phase-lagged SST and related TFLX. In addition to the phase lag in the diurnal processes, both Q1 and Q2 were weakened, associated with the reduced vertical advection of moisture. It is suggested that the phase-delayed diurnal cycle of SST greatly weakened the daytime convection and slightly enhanced the nighttime convection, resulting in a net reduction in daily mean state. Note that the shifted diurnal variations in heat/moisture in the CP6HC not only influenced the convection over the ocean but also overland, inducing an unrealistic diurnal cycle of precipitation (figures not shown).

In the uncoupled run, Q1 and Q2 were significantly reduced over 0.1 K/hr, associated with the weakening in vertical advection (Figure 10). Whats more, the positive anomalies in horizontal moisture advection (q_{vadv}) also indicated that the eastward moisture transport was reduced, which consisted of the easterly moisture flux anomalies, as shown in Figure 4g. As a result, the atmosphere became warmer (cooler) and drier (moister) during the daytime (nighttime) in NOCPC (Figure 10c and 10d). In general, the results shown above suggested that the convection and diurnal heat/moisture processes were greatly modulated when using the daily mean SST; however, to investigate the roles of the mean SST and its diurnal cycle, further experiments were needed (see the discussion section).

5 Discussion

5.1 The role of the daily mean SST

In our model, WRF-only received the SST from ROMS. The SSTs in CP12HC, CP1DC, and NOCPC were >0.6 °C lower than those in the highly coupled experiments, which may therefore be the key factor in the weakened convective activities (e.g., Dipankar et al., 2019). To confirm this, two extra WRF-only experiments were carried out by using the same settings in NOCPC but with modified SSTs. In NOCPC+, we replaced the OISST with the daily mean SST obtained from CP1HC within the Sumatra region (red box in Figure 1a), and such replacement was applied everywhere in the model domain in NOCPC++. One may notice that the SST in NOCPC+/NOCPC++ was slightly lower than that in CP1HC, which induced the linear interpolation of the daily mean SST into the 6-hourly SST, following the same procedure for the OISST in NOCPC. Fortunately, our results show that the biases were small and negligible (~ 0.02 °C, Table 2). Note that we only discussed the role of daily mean SST based on NOCPC++, and readers may refer to Section S2 in the Supporting Information for more results of the local SSTs.

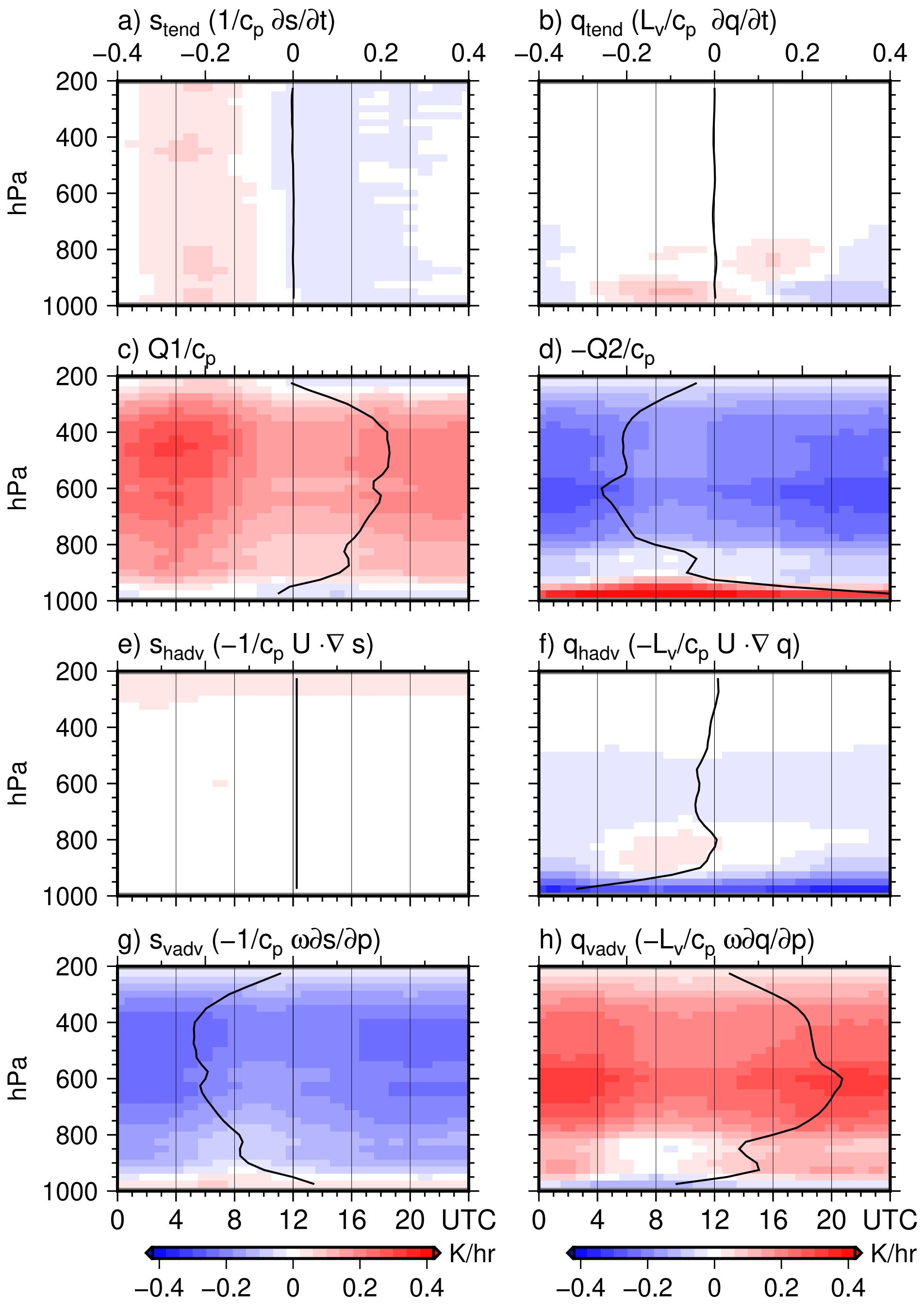

Figure 8. Diurnal composites of (a) tendency term, (c) apparent heat source Q1, (e) horizontal advection term, and (g) vertical advection term. Panels (b), (d), (f) and (h) are the same but for the moisture budget. The vertical distribution of daily mean values is also shown in each panel.

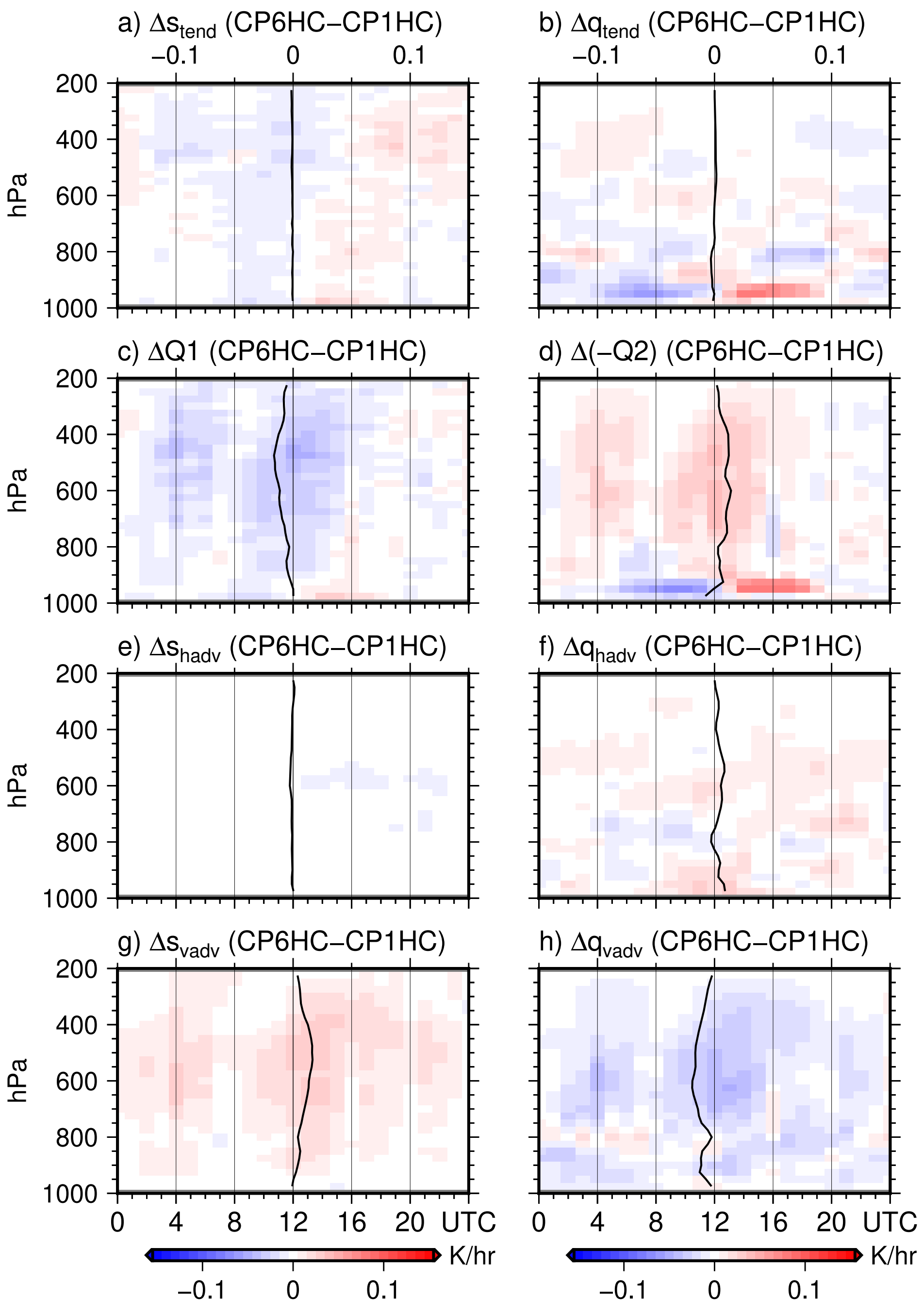

Figure 9. Same as in Figure 8 but for the differences between CP6HC and CP1HC.

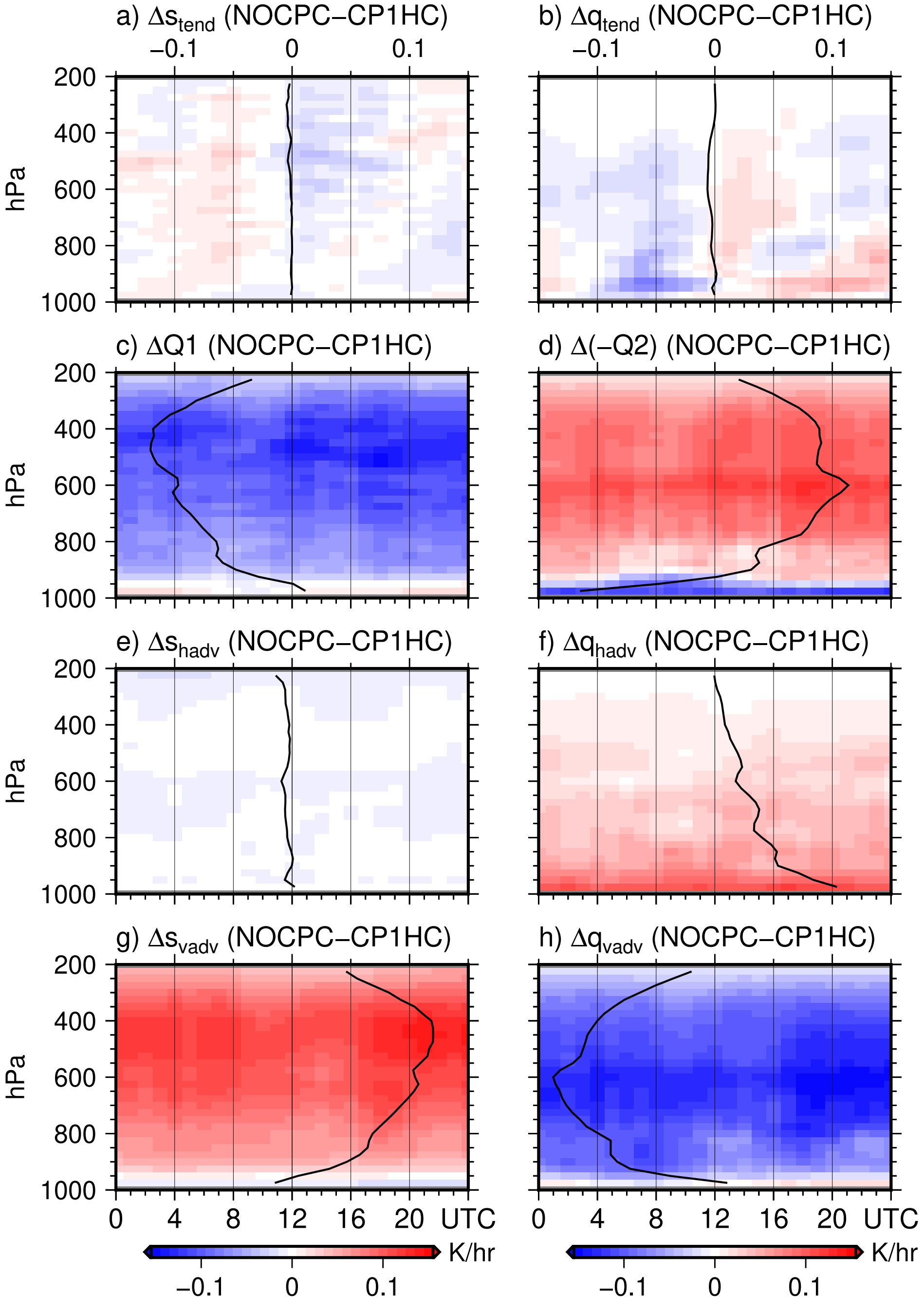

Figure 10. Same as in Figure 8 but for the differences between NOCPC and CP1HC.

In general, the higher SST induced the higher TFLX (Table 2 and Figure 7), more active convection (Figure 6), and therefore a moister atmosphere (Figure 4), which was almost comparable with those in highly coupled experiments. Whats more, with the same daily varying SST, the time evolution of convective activities also showed good agreements with the highly coupled models during the MJO. The anticyclonic gyre-like pattern of moisture flux anomalies remained, along with the small but negative biases in PW, although its center moved to the south. It is suggested that the underestimation of convection remained in NOCPC++, even with the same daily mean SST.

As showed in Figure 11, both Q1 and Q2 had small but nonnegligible negative anomalies from the surface to the midlevels. Moreover, unlike the monotonic reductions in NOCPC, the differences in NOCPC++ showed more subdaily variations. We found that the lower (higher) SST induced a drier (moister) boundary layer in NOCPC++ during the daytime (nighttime). Previous studies suggested that the premoistening of the lower troposphere is an important feature that can promote deep convection (Shinoda & Uyeda, 2002; Katsumata et al., 2018). Therefore, it is likely that this weakened moistening in the lower levels of NOCPC++ (approximately 5:00-12:00 UTC, Figure 11b) suppressed the onset of the subsequent diurnal deep convection, resulting in the negative Q1/Q2 and related vertical advection.

Based on the results of CP6HC and NOCPC++, the daily mean SST did play a dominant role in controlling the convection intensity, while the higher daytime SST (hence, the diurnal cycle of SST) played a smaller but nonnegligible role in daytime moistening and therefore the onset of diurnal deep convection. Figure 12 further demonstrates the above conclusion that while the higher daily mean SST induced larger moisture convergence, small but clear negative biases could be seen after 8:00 UTC in NOCPC++ and CP6HC, exhibiting weakened diurnal convection.

5.2 Modulations in the upper ocean

Since we found that the diurnal cycle of SST played a smaller role than the higher SST, one may ask why the highly coupled experiments had higher SSTs. To answer this question, we focused on the modulations in the ocean by air-sea coupling, especially the dynamics of the oceanic mixed layer and upper isothermal layer.

In this study, we defined the oceanic mixed-layer depth (MLD) in terms of a depth with a density equal to that at the 1 m depth plus an increment in density equivalent to -0.2 °C (Moteki et al., 2018), and therefore, the isotherm depth (ILD) is defined as the depth where the temperature is 0.2 °C lower than that at 1 m depth. Note that the results were not significantly changed when the reference depth was set to 10 m.

As shown in Figure 7c, the mixed-layer temperature (MLT, vertically averaged within the mixed layer) in the highly coupled experiments was approximately 29.0 °C, which was 0.8 °C (0.6 °C) higher than that in CP12HC (CP1DC). Both MLT and MLD had a weak but clear diurnal cycle, indicating the existence of stratification and destratification induced by the surface heating/cooling and mixing processes. The mixed layer became warmer and shallower after the sea surface was heated during the daytime (Figure 13a), and the largest MLT appeared 2 to 3 hours after the SST reached its maximum (Figure 7a), which was the time required by the adjustment processes (Figure 13d). Similar diurnal variations were found in ILDs, although it was generally over 10 m deeper than the MLD in all coupled experiments (Figures 13a).

Our results suggested that the mixed layer dynamics could be greatly modulated with or without high-frequency air-sea coupling. In barely coupled experiments, the MLTs were relatively higher than the SSTs (Figure 7a) because the ocean experienced net heat loss at the sea surface throughout the day (Figure 13c and Table 3). It is reasonable to consider that continuous surface cooling reduced the SST and broke down the upper layer

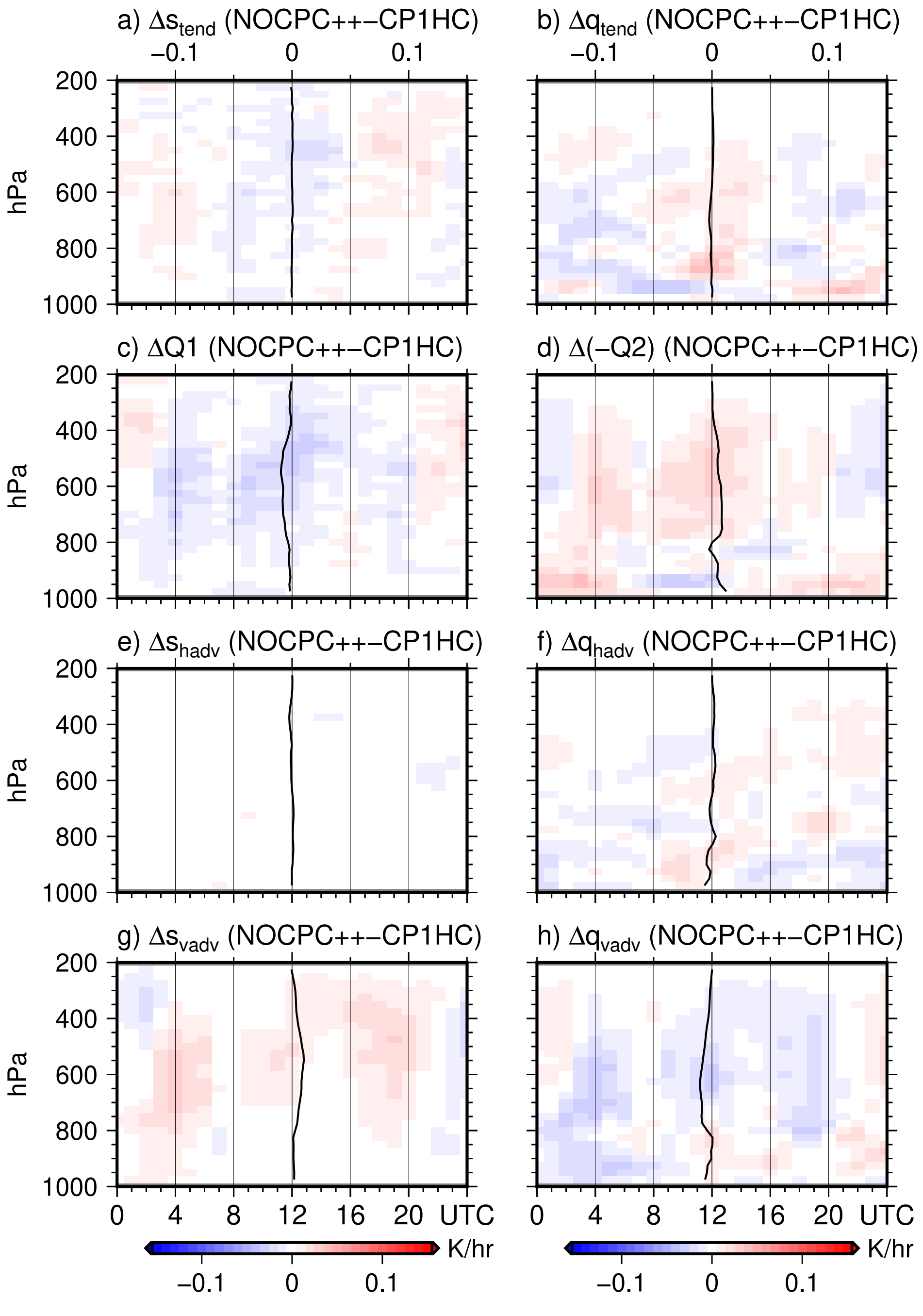

Figure 11. Same as in Figure 8 but for the differences between NOCPC++ and CP1HC.

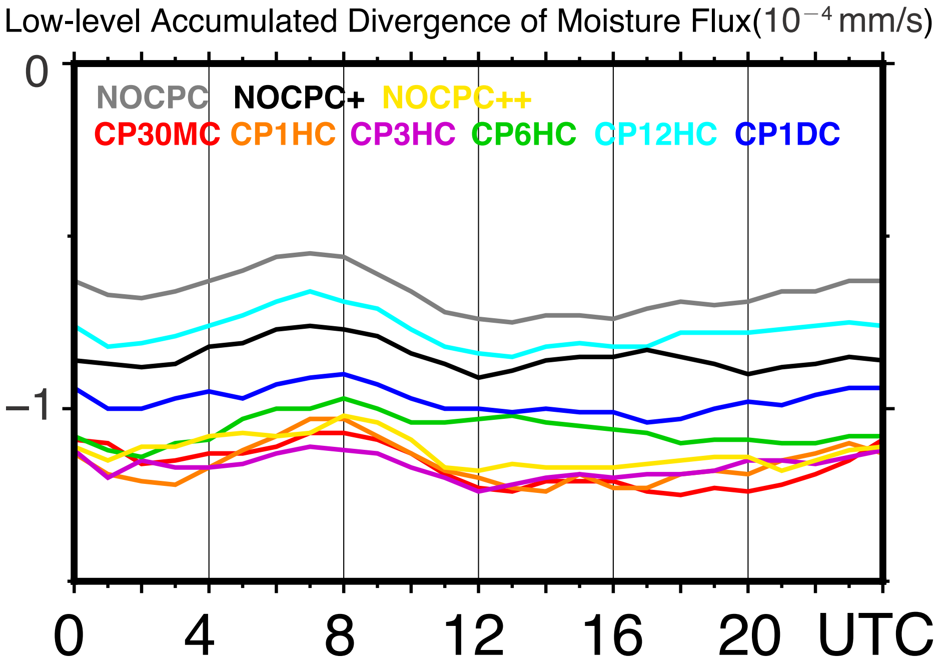

Figure 12. Diurnal composites of frequencies (occurrences) of the high RH (> 70%) around the Sumatra region (90°-110°E, 10°S-10°N; red box in Figure 1) at the (a) 700-hPa level; and (b) 500-hPa level.

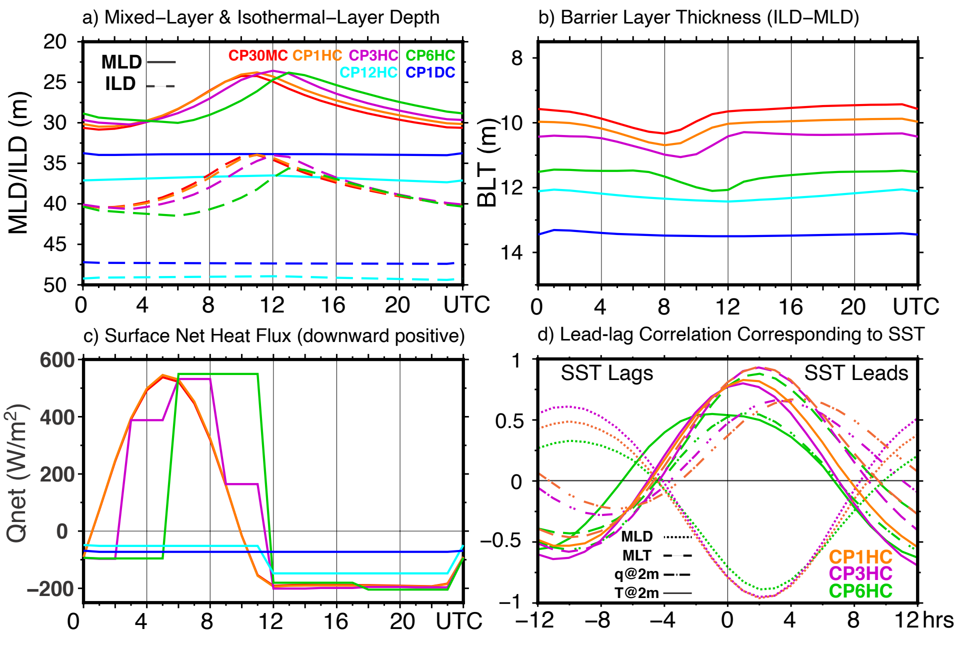

Figure 13. Diurnal composites of (a) the mixed-layer (solid line) and isothermal-layer depth (dashed line), (b) thicknesses of the barrier layer, and (c) the net heat flux at the sea surface (downward positive). (d) The lead-lag correlations of mixed-layer depth (dotted line), mixed-layer temperature (dashed line), surface air temperature (solid line), and specific humidity (dash-dotted line) corresponding to the SST.

Table 3. Daily Mean of Properties in ROMS

Experiment	MLT (°C)	MLD (m)	ILD (m)	BL (m)	Net Heat Flux at Sea Surface (W/m^2)
CP30MC	28.98	28.17	37.89	9.72	27.27
CP1HC	28.98	27.78	37.89	1011	28.15
CP3HC	28.97	27.54	38.05	10.51	24.65
CP6HC	28.91	27.56	39.18	11.62	17.54
CP12HC	28.23	36.86	49.11	12.25	-99.64
CP1DC	28.41	33.90	47.35	13.45	-72.49

instability, inducing strong vertical mixing and therefore the deepening of MLD/ILDs. Whats more, the deeper MLD further reduced the MLT. On the other hand, in highly coupled experiments, the net heat gain during the daytime would raise the SST and enhance the stratification that suppresses the mixing, leading to a shallower MLD/ILD. It is easy to find that the high-frequency air-sea coupling helped to maintain the higher SSTs/MLTs and shallower MLDs/ILDs.

Note that although all highly coupled experiments had similar mixed-layer processes (Figure 15d), the MLD (ILD) became relatively deeper (shallower) when the coupling frequency was higher (Table 3), inducing a thinner barrier layer (Figure 13b).

5.3 The drift of SST

Although the higher mean SST was generated by diurnal surface heating/cooling in highly coupled experiments, the SSTs may still be overestimated because of the positive biases from the OISST (satellite-based). On the other hand, as mentioned in previous studies, the OISST generally underestimates the true SST due to spatial smoothing and the removal of diurnal variations (Reynolds et al., 2007; Clayson & Bogdanoff, 2013). Therefore, it is necessary to compare them with the *in situ* observations. In this study, we used the SST measured by the *Mirai* Surface Meteorological observation (SMet) system at 5-m depth (SBE38, SeaBird Electronics). Details of the ship-based observations can be found in the MIRAI MR17-08 Cruise report (JAMSTEC & BPPT, 2018).

Figure 14 shows the time series of SSTs obtained in our models, satellite, and R/V *Mirai* during the active phase of the MJO, together with the precipitation rate observed by the optical rain gauge (ORG-815DR, Osi). The OISST (NOCPC) showed negative biases most times, while the models overestimated in some periods. The overestimation of SST on November 28th was mainly related to heavy rainfall, while the period from December 3rd was related to the underestimation of convection and its related precipitation (hence, surface cooling) as showed in Figures 3e and 3f. Nevertheless, both OISST and our modeled SSTs generally followed the trend of *in situ* observations in the same order. In addition, despite the slight underestimation of convection, our model showed good agreement with both satellite-based and *in situ* observations over the entire domain. Therefore, our conclusions on the importance of high-frequency air-sea coupling (and the higher and diurnally varying SST generated by that) are robust and reliable.

6 Concluding Remarks

A regional cloud-resolving coupled model was conducted to evaluate the impact of coupling frequency on convective activities during an MJO event captured in the YMC-Sumatra 2017 field campaign. By activating the scale-aware GFE cumulus scheme, the 1-hourly coupled model showed good agreements with both satellite-based precipitation and *in situ* radiosonde observations. Thus, a set of sensitivity experiments was carried

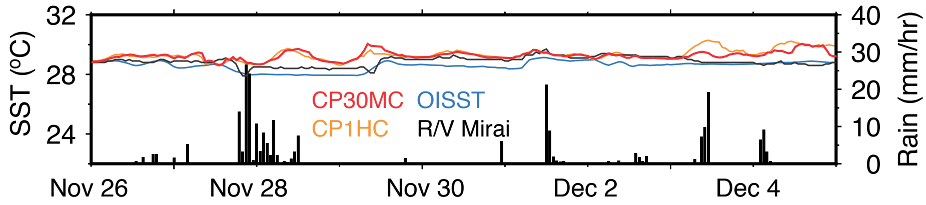

Figure 14. Time series of SSTs simulated/observed during the active phase of the MJO along with the observed precipitation rate by the R/V *Mirai*.

out to investigate the impact of the air-sea coupling frequency on convective activities during the MJO.

By varying the coupling frequency from 30 minutes to 1 day, we found that the PW in the atmosphere was largely reduced in the barely coupled experiments (12-hourly or daily coupled), associated with the westerly moisture flux anomalies (CP12HC and CP1DC; Figure 4). Our analysis indicated that the occurrences of high RH (>70%) were significantly reduced in the barely coupled experiments, especially at the 500-hPa level (middle troposphere), suggesting that deep convection was suppressed. Such a reduction occurred only after the MJO entered its active phase (Figure 6). Similar results were found in the uncoupled (atmosphere-only) model (NOCPC). The analysis of the apparent heat source (Q1) and moisture sink (Q2) budget confirmed that the vertical advection of heat and moisture played the dominant role during the active phase of the MJO, but both were weakened in the barely coupled and uncoupled experiments.

According to our results, high-frequency air-sea coupling is necessary for representing the diurnal cycle and the daily mean of SST. Specifically, in 30-minute and 1-hour coupled experiments (CP30MC and CP1HC), the SST successfully reproduced the diurnal cycle of SST, and the maximum SST appeared at 8:00 UTC, which consisted with observations (Ruppert & Johnson, 2015). However, in CP3HC (CP6HC), the time of the diurnal maximum SST was delayed by 1 hour (3 hours), and such phase lags were also found in surface turbulent heat fluxes (TFLX, Figure 7). The surface air temperature (T2m) and specific humidity (q2m) basically followed the same trend of SST in the highly coupled experiments (with few hours lagged), except in CP6HC where the T2m increased simultaneously with the SST (Figure 7 and 14b). Overall, the SST and TFLX had similar daily means in the highly coupled experiments but became lower in the barely coupled and uncoupled experiments.

To evaluate the role of the daily mean SST and its diurnal cycle, we conducted an extra WRF-only experiment (NOCPC++) by using the same daily mean SST from the 1-hourly coupled model. The results suggested that the mean SST did play the dominant role in promoting convection; however, the higher daytime SST (i.e., the diurnal cycle) also helped in moistening the lower troposphere, which is important for triggering deep convection. As a result, convection was still suppressed in NOCPC++ compared with CP1HC, even with the same daily mean SST.

In addition to the modulations in the atmosphere, our study also revealed the role of the coupling frequency in the upper ocean processes. We found that high-frequency air-sea coupling helped the maintenance of shallower mixed and isothermal layers by diurnal surface heating and cooling, leading to higher surface and upper layer temperatures (e.g., Shinoda 2005) and therefore stronger convection.

Overall, in comparison with previous studies (e.g., Seo et al., 2014), our study presented more detailed information on the subdaily modulations by the air-sea coupling frequency. Our results demonstrated the critical role of high-frequency coupling in representing both diurnal convection and upper ocean features since they were highly coupled with each other. Whats more, although our study focused on one specific MJO event and covered only two weeks, it is reasonable to consider that the impact of air-sea coupling may become more significant in a long-term simulation/prediction. Thus, further examination of long-term simulation and other MJO events will be a topic of ongoing study, together with experiments for resolution dependency (Holloway et al., 2015).

Acknowledgments

The authors are grateful to all those who engaged in the YMC-Sumatra 2017 field campaign, and the observational dataset is available at (`www.jamstec.go.jp/ymc/jpn/ymcj_data.html`). We also thank the following institutions/agencies for data provision: Japan Aerospace Exploration Agency for the GSMaP dataset, the National Centers for Environmental Pre-diction for the NCEP-FNL dataset, the National Centers for Environmental Information for the OISST dataset, the HYbrid Coordinates Ocean Model (HYCOM) Consortium for Data-Assimilative Ocean Modeling for the GOFS3.1 dataset, the U.S. Geological Survey for the GMTED2010 data, and the Bureau of Meteorology, Australia, for the RMM MJO index. This numerical experiments in this study were carried out on the JAMSTEC Super Computer System (DA System).

References

Amante, C., & Eakins, B. (2009). *1 arc-minute global relief model: Procedures, data sources, and analysis (ETOPO1)* [NOAA Technical Memorandum NESDIS NGDC-24]. Maryland, United States. (Accessed on 13 May, 2019) doi: 10.7289/V5C8276M

Bae, S., Hong, S.-Y., & Tao, W. (2018). Development of a single-moment cloud microphysics scheme with prognostic hail for the weather research and forecasting (WRF) model. *Asia-Pacific Journal of Atmospheric Sciences*, *55*, 233-245. doi: 10.1007/s13143-018-0066-3

Banzon, V., Smith, T. M., Chin, T. M., Liu, C., & Hankins, W. (2016). A long-term record of blended satellite and in situ sea-surface temperature for climate monitoring, modeling and environmental studies. *Earth System Science Data*, *8*(1), 165-176. doi: 10.5194/essd-8-165-2016

Chen, X., & Zhang, F. (2019). Relative roles of preconditioning moistening and global circumnavigating mode on the MJO convective initiation during DYNAMO. *Geophysical Research Letters*, *46*(2), 1079-1087. doi: 10.1029/2018GL080987

Clayson, C. A., & Bogdanoff, A. S. (2013). The effect of diurnal sea surface temperature warming on climatological air-sea fluxes. *Journal of Climate*, *26*(8), 2546-2556. doi: 10.1175/JCLI-D-12-00062.1

Crueger, T., Stevens, B., & Brokopf, R. (2013). The Madden-Julian oscillation in ECHAM6 and the introduction of an objective MJO metric. *Journal of Climate*, *26*(10), 3241-3257. doi: 10.1175/JCLI-D-12-00413.1

Cummings, J. A. (2005). Operational multivariate ocean data assimilation. *Quarterly Journal of the Royal Meteorological Society*, *131*(613), 3583-3604. doi: 10.1256/qj.05.105

Danielson, J. J., & Gesch, D. B. (2011). *Global multi-resolution terrain elevation data 2010 (GMTED2010)* [Open-File Report 20111073]. Virginia, United States. (Accessed on 13 May, 2019)

DeMott, C. A., Klingaman, N. P., & Woolnough, S. J. (2015). Atmosphere-ocean coupled processes in the Madden-Julian oscillation. *Reviews of Geophysics*, *53*(4), 1099-1154. doi: 10.1002/2014RG000478

Dipankar, A., Webster, S., Huang, X.-Y., & Doan, V. Q. (2019). Understanding biases in simulating the diurnal cycle of convection over the western coast of Sumatra: Comparison with pre-YMC observation campaign. *Monthly Weather Review*, *147*, 1615-1631. doi: 10.1175/MWR-D-18-0432.1

Fu, X., Lee, J.-Y., Hsu, P.-C., Taniguchi, H., Wang, B., Wang, W., & Weaver, S. (2013). Multi-model MJO forecasting during DYNAMO/CINDY period. *Climate Dynamics*, *41*, 1067-1081. doi: 10.1007/s00382-013-1859-9

Gerard, L. (2007). An integrated package for subgrid convection, clouds and precipitation compatible with meso-gamma scales. *Quarterly Journal of the Royal Meteorological Society*, *133*(624), 711-730. doi: 10.1002/qj.58

Green, B. W., Sun, S., Bleck, R., Benjamin, S. G., & Grell, G. A. (2017). Evaluation of MJO predictive skill in multiphysics and multimodel global ensembles. *Monthly Weather Review*, *145*(7), 2555-2574. doi: 10.1175/MWR-D-16-0419.1

Grell, G. A., & Freitas, S. R. (2014). A scale and aerosol aware stochastic convective parameterization for weather and air quality modeling. *Atmospheric Chemistry and Physics*, *14*(10), 5233–5250. doi: 10.5194/acp-14-5233-2014

Hagos, S., Leung, L. R., & Dudhia, J. (2011). Thermodynamics of the Madden-Julian oscillation in a regional model with constrained moisture. *Journal of the Atmospheric Sciences*, *68*(9), 1974-1989. doi: 10.1175/2011JAS3592.1

Hagos, S., Zhang, C., Feng, Z., Burleyson, C. D., DeMott, C., Kerns, B., ... Martini, M. N. (2016). The impact of the diurnal cycle on the propagation of Madden-Julian oscillation convection across the Maritime Continent. *Journal of Advances in Modeling Earth Systems*, *8*(4), 1552-1564. doi: 10.1002/2016MS000725

Holloway, C. E., Woolnough, S. J., & Lister, G. M. S. (2015). The effects of explicit versus parameterized convection on the MJO in a large-domain high-resolution tropical case study. part II: Processes leading to differences in MJO development. *Journal of the Atmospheric Sciences*, *72*(7), 2719-2743. doi: 10.1175/JAS-D-14-0308.1

Hong, S.-Y., & Jang, J. (2018). Impacts of shallow convection processes on a simulated boreal summer climatology in a global atmospheric model. *Asia-Pacific Journal of Atmospheric Sciences*, *54*(5), 361-370. doi: 10.1007/s13143-018-0013-3

Hong, S.-Y., Noh, Y., & Dudhia, J. (2006). A new vertical diffusion package with an explicit treatment of entrainment processes. *Monthly Weather Review*, *134*(9), 2318-2341. doi: 10.1175/MWR3199.1

Iacono, M. J., Delamere, J. S., Mlawer, E. J., Shephard, M. W., Clough, S. A., & Collins, W. D. (2008). Radiative forcing by long-lived greenhouse gases: Calculations with the AER radiative transfer models. *Journal of Geophysical Research: Atmospheres*, *113*(D13103). doi: 10.1029/2008JD009944

JAMSTEC, & BPPT. (2018). *Study on air-sea interaction over upwelling region in the eastern Indian Ocean* [R/V Mirai Cruise Report MR17-0]. Retrieved from `http://www.godac.jamstec.go.jp/catalog/data/doc_catalog/media/MR17-08_leg1-2_all.pdf`

Jimnez, P. A., Dudhia, J., Gonzlez-Rouco, J. F., Navarro, J., Montvez, J. P., & Garca-Bustamante, E. (2012). A revised scheme for the WRF surface layer formulation. *Monthly Weather Review*, *140*(3), 898-918. doi: 10.1175/MWR-D-11-00056.1

Katsumata, M., Mori, S., Hamada, J.-I., Hattori, M., Syamsudin, F., & Yamanaka, M. D. (2018). Diurnal cycle over a coastal area of the Maritime Continent as derived by special networked soundings over Jakarta during HARIMAU2010. *Progress in Earth and Planetary Science*, *5*(64). doi: 10.1186/s40645-018-0216-3

Kayano, M., & Kousky, V. (1999). Intraseasonal (30-60 day) variability in the global tropics: Principal modes and their evolution. *Tellus A: Dynamic Meteorology*

and Oceanography, *51*(3), 373-386. doi: 10.3402/tellusa.v51i3.13459
Kessler, W. S. (2001). EOF representations of the Madden-Julian oscillation and its connection with ENSO. *Journal of Climate*, *14*(13), 3055-3061. doi: 10.1175/1520-0442(2001)014⟨3055:EROTMJ⟩2.0.CO;2
Kim, H., Hoyos, C. D., Webster, P. J., & Kang, I.-S. (2010). Ocean-atmosphere coupling and the boreal winter MJO. *Climate Dynamics*, *35*, 771-784. doi: 10.1007/s00382-009-0612-x
Kim, H., Vitart, F., & Waliser, D. E. (2018). Prediction of the Madden-Julian oscillation: A review. *Journal of Climate*, *31*(23), 9425-9443. doi: 10.1175/JCLI-D-18-0210.1
Kwon, Y. C., & Hong, S.-Y. (2017). A mass-flux cumulus parameterization scheme across gray-zone resolutions. *Monthly Weather Review*, *145*(2), 583-598. doi: 10.1175/MWR-D-16-0034.1
Lorenz, D. J., & Hartmann, D. L. (2006). The effect of the MJO on the North American monsoon. *Journal of Climate*, *19*(3), 333-343. doi: 10.1175/JCLI3684.1
Madden, R. A., & Julian, P. R. (1972). Description of global-scale circulation cells in the tropics with a 40-50 day period. *Journal of the Atmospheric Sciences*, *29*(6), 1109-1123. doi: 10.1175/1520-0469(1972)029⟨1109:DOGSCC⟩2.0.CO;2
Madden, R. A., & Julian, P. R. (2005). Historical perspective. In W. K. M. Lau & D. E. Waliser (Eds.), *Intraseasonal variability in the atmosphere-ocean climate system* (p. 1-16). Springer-Praxis.
Mishra, S. K., Sahany, S., & Salunke, P. (2017). Linkages between MJO and summer monsoon rainfall over India and surrounding region. *Meteorology and Atmospheric Physics*, *129*(6), 283-296. doi: 10.1175/1520-0469(1972)029⟨1109:DOGSCC⟩2.0.CO;2
Morak-Bozzo, S., Merchant, C. J., Kent, E. C., Berry, D. I., & Carella, G. (2016). Climatological diurnal variability in sea surface temperature characterized from drifting buoy data. *Geoscience Data Journal*, *3*(1), 20-28. doi: 10.1002/gdj3.35
Mori, S., Jun-Ichi, H., Tauhid, Y. I., Yamanaka, M. D., Okamoto, N., Murata, F., ... Sribimawati, T. (2004). Diurnal landsea rainfall peak migration over Sumatera island, Indonesian Maritime Continent, observed by TRMM satellite and intensive rawinsonde soundings. *Monthly Weather Review*, *132*(8), 2021-2039. doi: 10.1175/1520-0493(2004)132⟨2021:DLRPMO⟩2.0.CO;2
Moteki, Q., Katsumata, M., Yoneyama, K., Ando, K., & Hasegawa, T. (2018). Drastic thickening of the barrier layer off the western coast of Sumatra due to the Madden-Julian oscillation passage during the pre-Years of the Maritime Continent campaign. *Progress in Earth and Planetary Science*, *5*(35). doi: 10.1186/s40645-018-0190-9
Nasuno, T. (2019). Moisture transport over the western Maritime Continent during the 2015 and 2017 YMC Sumatra campaigns in global cloud-system-resolving simulations. *SOLA*, *15*, 99-106. doi: 10.2151/sola.2019-019
Nasuno, T., Li, T., & Kikuchi, K. (2015). Moistening processes before the convective initiation of MaddenJulian oscillation events during the CINDY2011/DYNAMO period. *Monthly Weather Review*, *143*(2), 622-643. doi: 10.1175/MWR-D-14-00132.1
NCEP. (2000). *NCEP FNL Operational model global tropospheric analyses, continuing from July 1999.* Boulder CO: Research Data Archive at the National Center for Atmospheric Research, Computational and Information Systems Laboratory. Retrieved from `https://doi.org/10.5065/D6M043C6` (Accessed on 24 May, 2019) doi: 10.5065/D6M043C6
Neale, R., & Slingo, J. (2003). The Maritime Continent and its role in the global climate: A GCM study. *Journal of Climate*, *16*(5), 834-848. doi: 10.1175/1520-0442(2003)016⟨0834:TMCAIR⟩2.0.CO;2

Peatman, S. C., Matthews, A. J., & Stevens, D. P. (2014). Propagation of the Madden-Julian oscillation through the Maritime Continent and scale interaction with the diurnal cycle of precipitation. *Quarterly Journal of the Royal Meteorological Society*, *140*(680), 814-825. doi: 10.1002/qj.2161

Pilon, R., Zhang, C., & Dudhia, J. (2016). Roles of deep and shallow convection and microphysics in the MJO simulated by the model for prediction across scales. *Journal of Geophysical Research: Atmospheres*, *121*(18), 10,575-10,600. doi: 10.1002/2015JD024697

Raymond, D. J., & Fuchs, Ž. (2009). Moisture modes and the Madden-Julian oscillation. *Journal of Climate*, *22*(11), 3031-3046. doi: 10.1175/2008JCLI2739.1

Reynolds, R. W., Smith, T. M., Liu, C., Chelton, D. B., Casey, K. S., & Schlax, M. G. (2007). Daily high-resolution-blended analyses for sea surface temperature. *Journal of Climate*, *20*(22), 5473-5496. doi: 10.1175/2007JCLI1824.1

Ruppert, J. H., & Johnson, R. H. (2015). Diurnally modulated cumulus moistening in the preonset stage of the Madden-Julian oscillation during DYNAMO. *Journal of the Atmospheric Sciences*, *72*(4), 1622-1647. doi: 10.1175/JAS-D-14-0218.1

Seo, H., Subramanian, A. C., Miller, A. J., & Cavanaugh, N. R. (2014). Coupled impacts of the diurnal cycle of sea surface temperature on the Madden-Julian oscillation. *Journal of Climate*, *27*(22), 8422-8443. doi: 10.1175/JCLI-D-14-00141.1

Shinoda, T. (2005). Impact of the diurnal cycle of solar radiation on intraseasonal SST variability in the western Equatorial Pacific. *Journal of Climate*, *18*(14), 2628-2636. doi: 10.1175/JCLI3432.1

Shinoda, T., & Uyeda, H. (2002). Effective factors in the development of deep convective clouds over the wet region of eastern China during the summer monsoon season. *Journal of the Meteorological Society of Japan. Ser. II*, *80*(6), 1395-1414. doi: 10.2151/jmsj.80.1395

Tewari, M., Chen, F., Wang, W., Dudhia, J., LeMone, M., Mitchell, K., ... Cuenca, R. (2004). *Implementation and verification of the unified NOAH land surface model in the WRF model.* Presentation. Seattle, WA, US..

Tseng, K.-C., Sui, C.-H., & Li, T. (2015). Moistening processes for Madden-Julian oscillations during DYNAMO/CINDY. *Journal of Climate*, *28*(8), 3041-3057. doi: 10.1175/JCLI-D-14-00416.1

Vitart, F. (2014). Evolution of ECMWF sub-seasonal forecast skill scores. *Quarterly Journal of the Royal Meteorological Society*, *140*(683), 1889-1899. doi: 10.1002/qj.2256

Waliser, D. E., Lau, K. M., & Kim, J.-H. (1999). The influence of coupled sea surface temperatures on the Madden-Julian oscillation: A model perturbation experiment. *Journal of the Atmospheric Sciences*, *56*(3), 333-358. doi: 10.1175/1520-0469(1999)056⟨0333:TIOCSS⟩2.0.CO;2

Wang, B., & Moon, J.-Y. (2018). Subseasonal prediction of extreme weather events. In H.-S. Jung & B. Wang (Eds.), *Bridging science and policy implication for managing climate extremes* (p. 33-48). World Scientific. doi: 10.1142/9789813235663_0003

Warner, J. C., Armstrong, B., He, R., & Zambon, J. B. (2010). Development of a coupled ocean-atmosphere-wave-sediment transport (COAWST) modeling system. *Ocean Modelling*, *35*(3), 230-244. doi: https://doi.org/10.1016/j.ocemod.2010.07.010

Webber, B. G. M., Matthews, A. J., & Heywood, K. J. (2010). A dynamical ocean feedback mechanism for the Madden-Julian oscillation. *Quarterly Journal of the Royal Meteorological Society*, *136*(648), 740-754. doi: 10.1002/qj.604

Wu, P., Ardiansyah, D., Mori, S., & Yoneyama, K. (2019, aug). The effect of an active phase of the Madden-Julian oscillation on surface winds over the western coast of Sumatra island. *IOP Conference Series: Earth and Environmental*

Science, *303*, 012009. doi: 10.1088/1755-1315/303/1/012009

Yokoi, S., Mori, S., Katsumata, M., Geng, B., Yasunaga, K., Syamsudin, F., … Yoneyama, K. (2017). Diurnal cycle of precipitation observed in the western coastal area of Sumatra island: Offshore preconditioning by gravity waves. *Monthly Weather Review*, *145*(9), 3745-3761. doi: 10.1175/MWR-D-16-0468.1

Yokoi, S., Mori, S., Syamsudin, F., Haryoko, U., & Geng, B. (2019). Environmental conditions for nighttime offshore migration of precipitation area as revealed by in situ observation off Sumatra island. *Monthly Weather Review*, *147*(9), 3391-3407. doi: 10.1175/MWR-D-18-0412.1

Zermeo-Daz, D. M., Zhang, C., Kollias, P., & Kalesse, H. (2015). The role of shallow cloud moistening in MJO and non-MJO convective events over the ARM Manus site. *Journal of the Atmospheric Sciences*, *72*(12), 4797-4820. doi: 10.1175/JAS-D-14-0322.1

Zhang, C. (2013). Madden-Julian oscillation: Bridging weather and climate. *Bulletin of the American Meteorological Society*, *94*(12), 1849-1870. doi: 10.1175/BAMS-D-12-00026.1

Zhang, C., & Anderson, S. P. (2003). Sensitivity of intraseasonal perturbations in SST to the structure of the MJO. *Journal of the Atmospheric Sciences*, *60*(17), 2196-2207. doi: 10.1175/1520-0469(2003)060⟨2196:SOIPIS⟩2.0.CO;2

Zhang, C., & Wang, Y. (2017). Projected future changes of tropical cyclone activity over the western North and south Pacific in a 20-km-mesh regional climate model. *Journal of Climate*, *30*(15), 5923-5941. doi: 10.1175/JCLI-D-16-0597.1

Zheng, Y., Alapaty, K., Herwehe, J. A., Del Genio, A. D., & Niyogi, D. (2016). Improving high-resolution weather forecasts using the weather research and forecasting (WRF) model with an updated Kain-Fritsch scheme. *Monthly Weather Review*, *144*(3), 833-860. doi: 10.1175/MWR-D-15-0005.1

Zhu, J., Wang, W., & Kumar, A. (2017). Simulations of MJO propagation across the Maritime Continent: Impacts of SST feedback. *Journal of Climate*, *30*(5), 1689-1704. doi: 10.1175/JCLI-D-16-0367.1

Supporting Information for "How does the air-sea coupling frequency affect convection during the MJO passage?"

Ning Zhao[1], Tomoe Nasuno[1]

[1]Japan Agency for Marine Earth Science and Technology, Yokosuka, Kanagawa, Japan

Contents of this file

1. Text S1 to S2
2. Figures S1 to S6
3. Table S1

Introduction There are two sections included in the supporting information. Section S1 shows the details of the sensitivity experiments for cumulus parameterizations (Table S1), and their results are presented by Figures S1 and S2. Figure S3 shows the time series of SSTs in the experiments, which mentioned in Section 4.1 of the main text. Section S2 mainly showed the additional results when the SST was increased locally within the Sumatra region (Figures S4, S5 and S6).

Text S1. For the use of Cumulus Parameterizations In this study, all the simulations were carried out based on 7-km mesh size, which is a so-called grey zone resolution that convection is partially resolved, partially sub-grid (Gerard, 2007). At this resolution, the effect of cumulus parameterization is somehow case-by-case. Therefore, we conducted five experiments with and without cumulus parameterizations to find the best model settings for this study (CP1H, CP1HC, CP1HC2, CP1HC3, and CP1HC4, see Table S1). All five experiments were carried out by the 1-hourly WRF-ROMS coupled model.

Especially, three cumulus schemes are scale-aware schemes, which were designed for the transition zone from the classical convection-permitting (<= 4km) and mesoscale (>= 10km) regime, including the Grell-Freitas Ensemble (GFE) scheme (Grell & Freitas, 2014), the New Simplified Arakawa-Schubert (NSAS) scheme (Kwon & Hong, 2017), and the Multi-scale Kain-Fritsch (MKF) scheme (Zheng et al., 2016). Furthermore, we also tested the New Tiedtke (NT) scheme (Zhang & Wang, 2017), which is not scale-aware but includes both deep and shallow cumulus components. Since the NSAS scheme in CP1HC3 does not have the shallow convection component, which was proved to be important in simulating convection (Pilon et al., 2016), we also applied the Global/Regional Integrated Model system (GRIMs) shallow convection scheme (Hong & Jang, 2018) following Kwon and Hong (2017).

Figure S1 shows the horizontal distributions of mean precipitation rates and maximum precipitation time during the active phase of MJO (Nov. 26th -Dec. 4th) obtained by satellite and five experiments. In general, all five simulations captured the fundamental precipitation structures but with different magnitudes. However, the heavy rainfall could only be found in CP1HC and CP1HC3, but underestimated in other experiments.

Figure S2 represents the horizontal maps of the UTC time when the maximum precipitation obtained from the GSMaP and five experiments. The maximum rainfall mainly occurred in the evening (about 12:00 UTC) over the largest islands in the study domain (i.e., Sumatra Island and Kalimantan Island) and in the early morning over the seas near the coast. Such patterns were successfully simulated in CP1H, CP1HC, and CP1HC4, but the rainfall occurred too early in CP1HC2 and CP1HC3, especially near the coast. Over the Indian Ocean, the nighttime maximum rainfall showed two band-like patterns, which is also well-simulated in CP1HC.

Text S2. Additional results for local SST In NOCPC++, we applied the daily mean SST from CP1HC in the whole domain, which affect both local and background conditions. For our own interests, we applied the higher SST only within the Sumatra region in NOCPC+ (90 110°E, 10°S 10°N; box in Figures 1 and S3), and by doing so, we could briefly evaluate the role of local SST in promoting the convection and the circulations on a larger scale.

Our results clearly showed that the increase of local SST reduced the drier bias within the Sumatra region, but the anti-cyclonic gyre-like moisture flux anomalies remained clear and strong (Figure 4h). The only two exceptions were found in the area east of the Malay Peninsula and the area near the Java Island, where the positive (moister) biases were found downstream of the Sumatra region.

Comparing with NOCPC, the increased mean SSTs enhanced the PW and moisture fluxes in NOCPC+ (Figure S4). The locally increased SST moistened the atmosphere southwest of Sumatra region, and the largest moisture anomalies appeared near the Java Island. The eastward jet-like moisture flux anomalies, associated with two cyclonic gyre-like patterns, were similar to the background conditions as showed in CP1HC (Figure 4a), but with smaller scales and magnitudes. Whats more, the locally increased SST also induced the northward moisture transport in the Southern Hemisphere, leading to the negative biases of PW. Interestingly, over the region of Andaman Sea (west of Malay

Peninsula), the atmosphere became drier than NOCPC, even the local SST was increased (see the black box in Figure S4a). As the SST increased over the entire domain (i.e., NOCPC++; Figure S4b), the aforementioned modifications remained and further be enhanced. The cyclonic gyre became much larger and stronger, although the center moved to the west of Andaman Sea inducing a small negative bias east of Malay Peninsula.

At the sea surface, the TFLX in NOCPC+ was largely increased and 32.8 W/m^2 higher than NOCPC, even the SST difference was only about 0.6 °C. As showed in Figure S5, the TFLX was mainly controlled by the latent heat flux (LH), which was one order larger than the sensible heat flux (SH). The increased LH helped the moistening of the atmospheric boundary layer and enhanced the development of deep convection (e.g., Katsumata et al., 2018), which can be seen by the reduction of negative biases in high RH from the surface to the upper troposphere (Figures 5g and 5h). However, such enhancement in moisture supply was relatively smaller in NOCPC+ due to the lower TFLX (LH), resulting in the larger negative biases of high RH (Figure 5h and 5i). Note that T2m in NOCPC+ was similar to that in highly coupled experiments or NOCPC++, consisting of the similar sensible heat fluxes found in these two experiments (Figure S5a).

Interestingly, we found that the increased local SST induced about half of the improvement in the local convection (compared to NOCPC++). For example, the low-level moisture convergence, which could be regarded as an indicator of convection, was increased about 0.25 $\times 10^{-4}$ mm/s comparing to NOCPC (Figure 12). Similar conclusion could be found from the heat and moisture budget analyses (Figure S6). Despite the similar sub-daily biases due to the lack of higher daytime SST (see the Subsection 5a), the higher local SST reduced at least half of the underestimation of moistening/heating processes (i.e., convective activities) in the model. Note that we used the word at least, because CP1HC also underestimated the convection as suggested by the in-situ observations (Figure 3).

References

Gerard, L. (2007). An integrated package for subgrid convection, clouds and precipitation compatible with meso-gamma scales. *Quarterly Journal of the Royal Meteorological Society*, *133*(624), 711-730. doi: 10.1002/qj.58

Grell, G. A., & Freitas, S. R. (2014). A scale and aerosol aware stochastic convective parameterization for weather and air quality modeling. *Atmospheric Chemistry and Physics*, *14*(10), 5233–5250. doi: 10.5194/acp-14-5233-2014

Hong, S., & Jang, J. (2018). Impacts of shallow convection processes on a simulated boreal summer climatology in a global atmospheric model. *Asia-Pacific Journal of Atmospheric Sciences*, *54*(5), 361-370. doi: 10.1007/s13143-018-0013-3

Katsumata, M., Mori, S., Hamada, J.-I., Hattori, M., Syamsudin, F., & Yamanaka, M. D. (2018). Diurnal cycle over a coastal area of the maritime continent as derived by special networked soundings over jakarta during harimau2010. *Progress in Earth and Planetary Science*, *5*(64). doi: 10.1186/s40645-018-0216-3

Kwon, Y. C., & Hong, S.-Y. (2017). A mass-flux cumulus parameterization scheme across gray-zone resolutions. *Monthly Weather Review*, *145*(2), 583-598. doi: 10.1175/MWR-D-16-0034.1

Pilon, R., Zhang, C., & Dudhia, J. (2016). Roles of deep and shallow convection and microphysics in the mjo simulated by the model for prediction across scales. *Journal of Geophysical Research: Atmospheres*, *121*(18), 10,575-10,600. doi:

10.1002/2015JD024697

Zhang, C., & Wang, Y. (2017). Projected future changes of tropical cyclone activity over the western north and south pacific in a 20-km-mesh regional climate model. *Journal of Climate*, *30*(15), 5923-5941. doi: 10.1175/JCLI-D-16-0597.1

Zheng, Y., Alapaty, K., Herwehe, J. A., Del Genio, A. D., & Niyogi, D. (2016). Improving high-resolution weather forecasts using the weather research and forecasting (wrf) model with an updated kain-fritsch scheme. *Monthly Weather Review*, *144*(3), 833-860. doi: 10.1175/MWR-D-15-0005.1

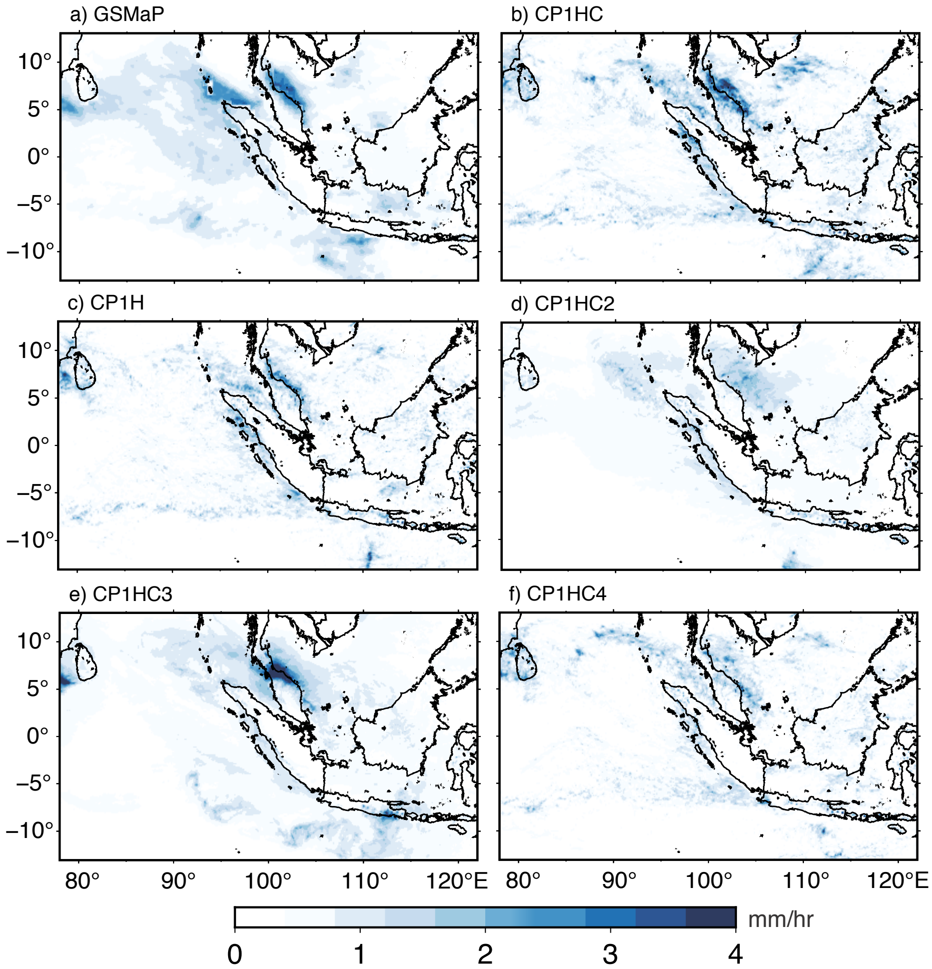

Figure S1. Horizontal distributions of the precipitation rates obtained from satellite observations and models with different cumulus parameterizations. (a) GSMaP; (b) CP1HC (GFE scheme); (c) CP1H (no cumulus scheme); (d) CP1HC2 (NT scheme); (e) CP1HC3 (NSAS + GRIMs scheme); and (f) CP1HC4 (MKF scheme). Note that, for ease to compare, panel S1a and S1b are identical to Figure 2a and 2b, respectively.

Table S1. Descriptions of the sensitivity experiments

Experiment	Cumulus Parameterization
CP1H	N/A
CP1HC	GFE scheme
CP1HC2	NT scheme
CP1HC3	NSAS + GRIMs scheme
CP1HC4	MKF scheme

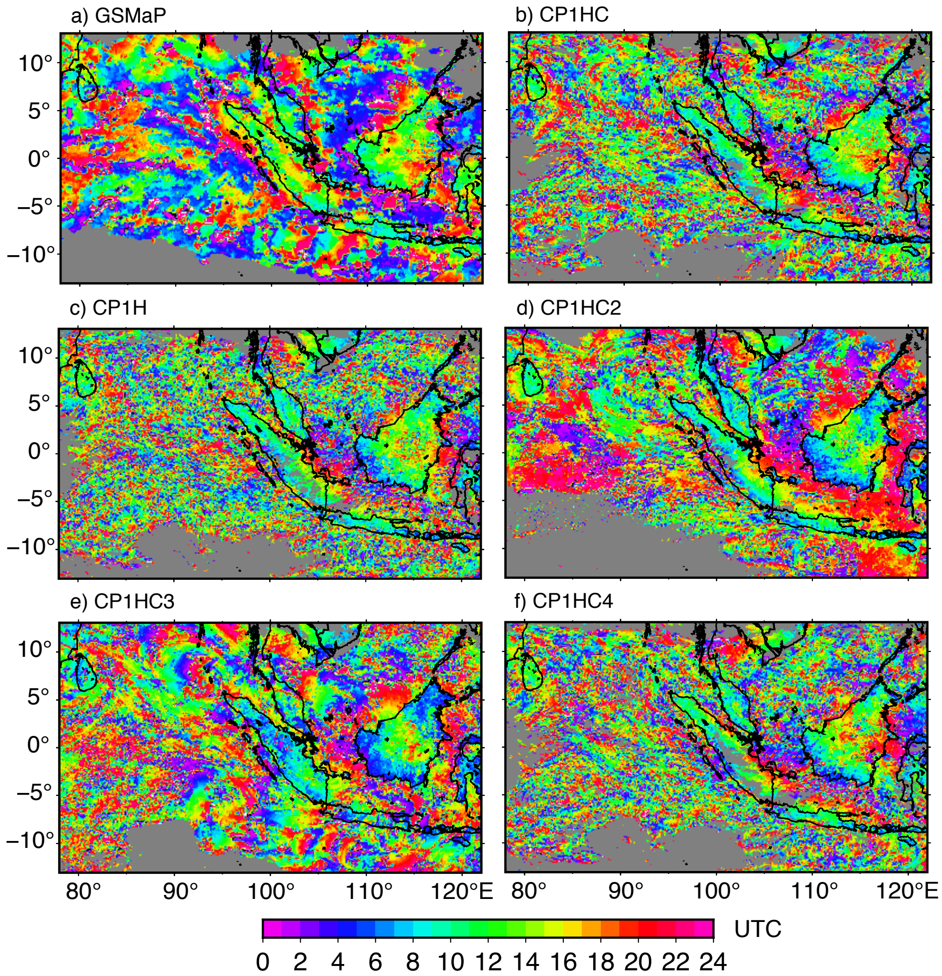

Figure S2. Same as Figure 2 but for the time of maximum precipitation (in UTC). Grids with weak precipitation (< 1 mm/hr) were excluded.

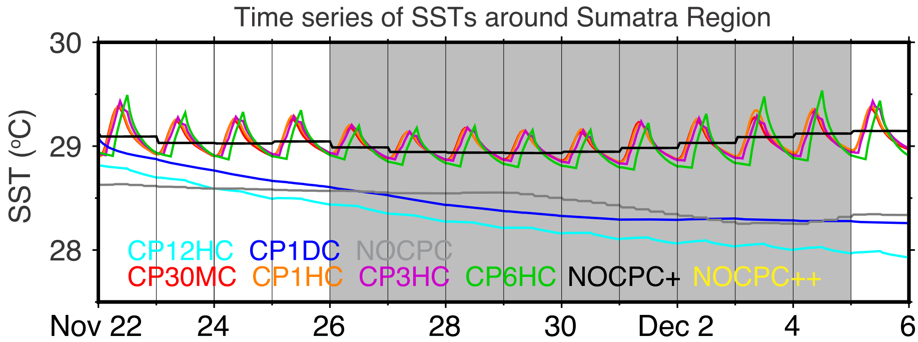

Figure S3. Same as Figure 6 but for the time series of SSTs. Note that the SSTs in NOCPC+ and NOCPC++ were identical, so that no yellow line can be seen.

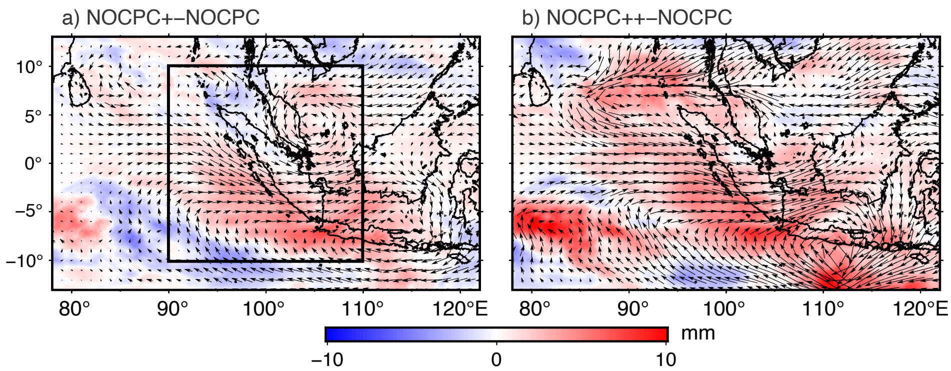

Figure S4. Improvement of the precipitable water and moisture fluxes during the active phase of MJO (November 26th to December 4th) in (a) NOCPC+ and (b) NOCPC++ in comparison with NOCPC. The Sumatra region is indicated by the black box in panel a, which is same as the red box in Figure 1.

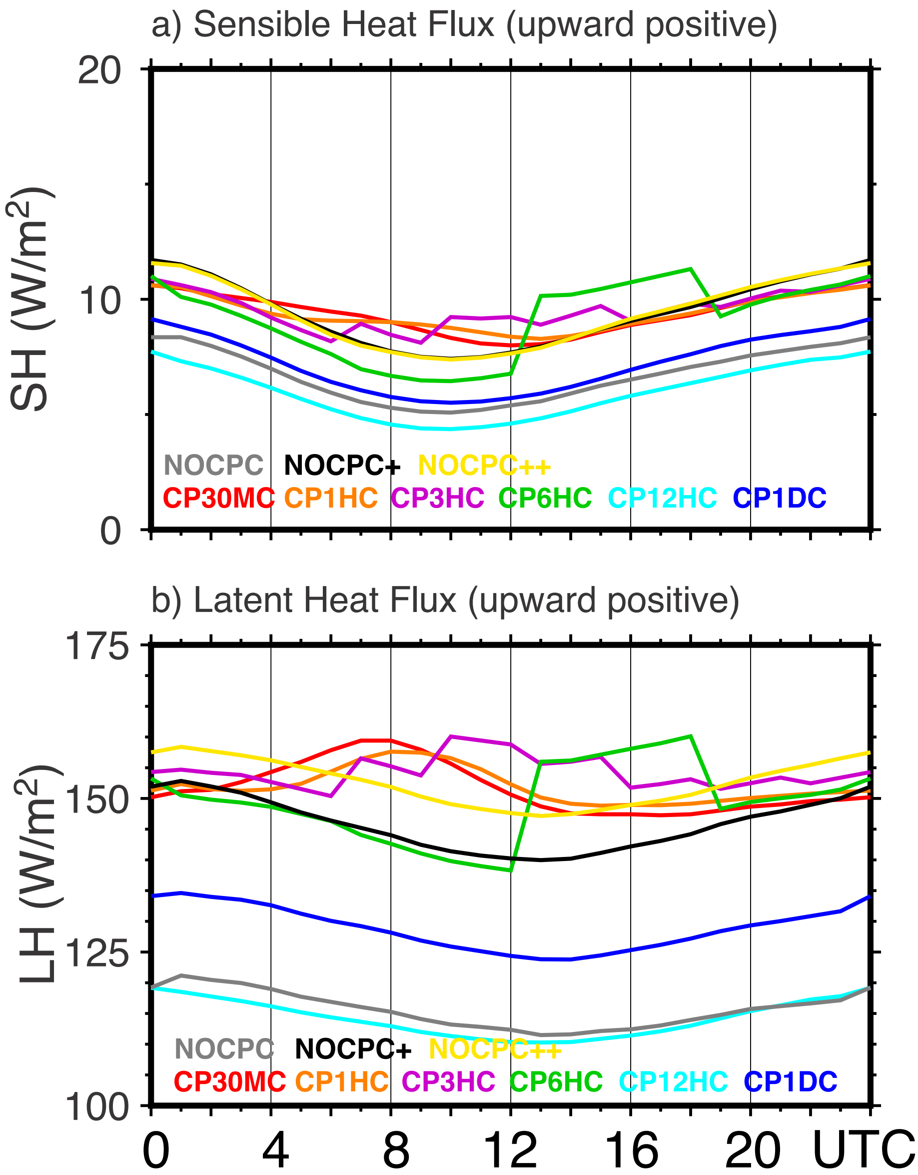

Figure S5. Diurnal composites of (a) the sensibile heat flux and (b) the latent heat flux. Positive value means atmosphere gains heat (i.e., upward positive).

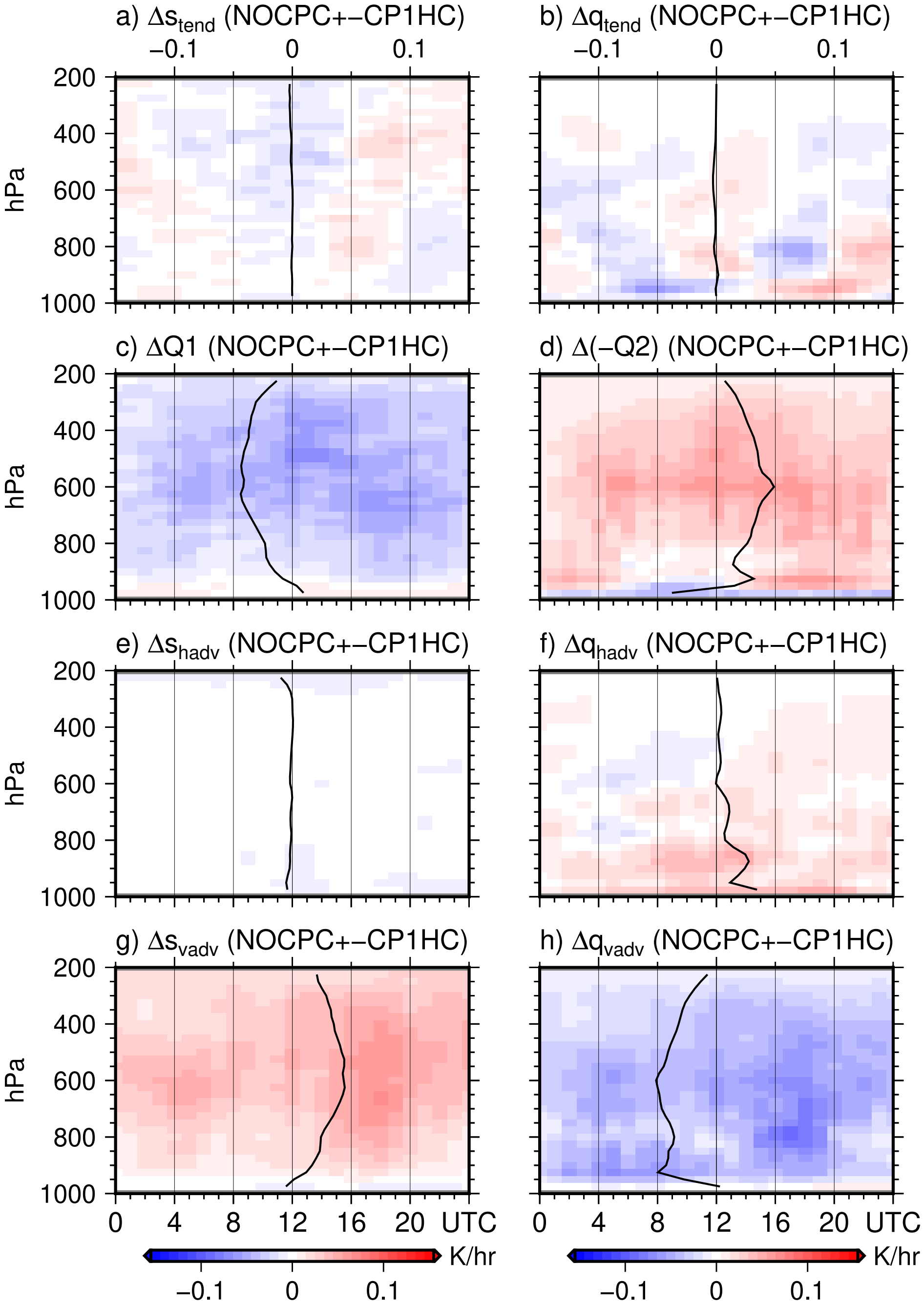

Figure S6. Diurnal composites of the differences in heat and moisture budget between NOCPC+ and CP1HC.